A Frequency-Dependent Description of Propagating Sea Level Signals in the Kuroshio Extension Region

HONGYANG LIN*

State Key Laboratory of Marine Environmental Science, College of Ocean and Earth Sciences, Xiamen University, Xiamen, Fujian, China

KEITH R. THOMPSON

Department of Oceanography, Dalhousie University, Halifax, Nova Scotia, Canada

JIANYU HU

State Key Laboratory of Marine Environmental Science, College of Ocean and Earth Sciences, Xiamen University, Xiamen, Fujian, China

(Manuscript received 21 August 2013, in final form 10 March 2014)

ABSTRACT

Hilbert empirical orthogonal function analysis is used to provide a frequency-dependent description of observed sea level variability in the Kuroshio Extension region, 1993–2012 inclusive. The dominant high-frequency mode (periods between 140 and 350 days) describes signals that propagate westward with the largest amplitudes in the vicinity of the Shatsky Rise and Emperor Seamounts. Based on the close correspondence between the variance of the high-frequency variability and the underlying bathymetry, it is speculated that this mode is driven by jet–bathymetry interactions. The dominant low-frequency mode (periods longer than 350 days) is explained in terms of wind-forced, jet-trapped Rossby waves that propagate along the mean Kuroshio Extension jet. One of the most surprising findings of this study is that sea level changes north of the jet in the meander region anticipate changes south of the jet by about 3 yr. Based on correlations of observed sea level with the Pacific decadal oscillation, and western boundary transport variability estimated from the Global Ocean Reanalysis and Simulations (GLORYS), it is speculated that this anticipation is due to the differences in time taken for (i) Rossby waves to travel from the eastern North Pacific to the meander region and (ii) the much faster barotropic response of western boundary transport, and sea level north of the jet, to large-scale forcing by the wind stress curl.

1. Introduction

The Kuroshio is the most prominent western boundary current of the North Pacific. After leaving the coast at 35°N, it flows eastward into the open ocean and becomes the Kuroshio Extension jet (e.g., Qiu 2002; Jayne et al. 2009). This midocean jet is unstable, and the resulting meanders and pinch-off eddies make the Kuroshio Extension one of the most energetic regions of the world's oceans (e.g., Aoki and Imawaki 1996; Ducet et al. 2000). Interest in the Kuroshio Extension is driven in part by practical issues such as variations in the productivity of local fisheries (e.g., Barkley 1970) and the tracks and intensity of storms in the western North Pacific (e.g., Nakamura et al. 2004). In addition, poleward heat transport by the Kuroshio has a significant impact on atmosphere–ocean interactions and is thus linked to larger-scale variations of the climate system (e.g., Yasuda 2003; Kwon et al. 2010). Another topic of great scientific and practical interest is the predictability of decadal variations in this region (Mochizuki et al. 2010).

The Kuroshio Extension region has been the subject of numerous modeling and observational studies. For example, Hurlburt et al. (1996) used a realistic model to

* Current affiliation: Dalhousie University, Halifax, Nova Scotia, Canada.

Corresponding author address: Dr. Jianyu Hu, College of Ocean and Earth Sciences, Xiamen University, 182 Daxue Road, Xiamen, Fujian 361005, China.
E-mail: hujy@xmu.edu.cn

DOI: 10.1175/JPO-D-13-0185.1

show that bathymetry, wind forcing, baroclinicity, and nonlinear processes all play important roles in determining the mean and variability of this current system. The underlying dynamical mechanisms have also been elucidated by observational studies including the recent Kuroshio Extension System Study (e.g., Jayne et al. 2009; Donohue et al. 2010). Taken together, the modeling and observational studies suggest that the Kuroshio Extension is a highly nonlinear system in which eddies and large-scale atmospheric forcing play important roles in controlling the mean state and also the variability (Waterman et al. 2011).

The Kuroshio Extension has been observed to vary over a wide range of time scales. In addition to vigorous eddy variability on time scales of weeks to months (e.g., Ebuchi and Hanawa 2000), the system exhibits significant low-frequency variability on times scales of years to decades. This variability has been detected in altimeter measurements of sea surface height (e.g., Qiu and Chen 2005; Sasaki et al. 2013) and radiometer measurements of sea surface temperature (e.g., Chen 2008) made over the last two decades.

The cause of the low-frequency variability remains controversial. Taguchi et al. (2007) noted two possible causes. The first is internally generated variability. Theoretical and modeling studies (e.g., McCalpin and Haidvogel 1996; Berloff and McWilliams 1999; Hogg et al. 2005) have shown that the ocean can generate its own low-frequency variability through nonlinear processes. The second is large-scale atmospheric forcing. There is strong evidence that a significant part of the low-frequency variability is driven by the large-scale wind stress curl and subsequent adjustment by Rossby waves (e.g., Qiu 2003; Taguchi et al. 2005). In an attempt to reconcile these two views, Taguchi et al. (2007) carried out a statistical analysis of observed and predicted sea level data for the Kuroshio Extension region. They concluded that large-scale wind variability generates westward-propagating Rossby waves that trigger ''intrinsic modes'' of the Kuroshio Extension jet leading to high-wavenumber variations of sea level in the vicinity of the jet.

Recently, Sasaki and Schneider (2011) and Sasaki et al. (2013) used the thin-jet theory of Cushman-Roisin et al. (1993) to show that meridional shifts of the Kuroshio Extension jet can propagate as long Rossby waves along the potential vorticity gradient of the mean jet. Thin-jet theory leads to three important conclusions: signals propagate westward along the jet at a speed comparable to that of nondispersive linear Rossby waves, they have a narrow meridional structure around the path of mean jet, and their amplitudes vary with the mean sea level drop across the jet. Sasaki et al. (2013) noted that all of these features are consistent with observations and cannot be predicted by traditional linear Rossby wave theory. They also noted that changes in the northern recirculation gyre lead the southern recirculation gyre by 6 months but did not provide a physical mechanism.

A variety of statistical techniques have been used to describe the variability observed in the Kuroshio Extension region. Empirical orthogonal function (EOF) analysis has been used to identify dominant modes of variability of the Kuroshio Extension path (e.g., Qiu et al. 1991). Wavenumber spectral analysis (e.g., Tai and White 1990) has been applied to altimeter observations to determine the dominant direction of phase propagation. Longitude–time lag correlation diagrams of sea level and sea surface temperature anomalies have been used to investigate their westward propagation and phase speed (Aoki et al. 1995). Wavelet transforms have been used to describe sea level propagation in the South Pacific (Wang et al. 1998b). Most of the above studies focused on propagation in one direction.

Hilbert empirical orthogonal function (HEOF) analysis is a dimension reduction technique that has been used widely in oceanic and atmospheric sciences to extract dominant propagating signals (e.g., Barnett 1983; Wang et al. 1998a; Cromwell 2006; Sheu et al. 2010). [Note that we have followed the recommendation of von Storch and Zwiers (1999) and used the expression Hilbert EOF, instead of the potentially confusing expression complex EOF.] HEOF analysis can provide information on propagation in more than one dimension and can be focused on specific frequency bands of interest. The technique has been used to describe variability in the Kuroshio Extension region. For example, Tracey et al. (2012) recently used HEOF analysis to describe the variability of meanders using surface geopotential height calculated from observations made by an extensive array of moorings deployed in the vicinity of the Kuroshio Extension jet. HEOF analysis has also been used to study observed sea level variability in the Kuroshio Extension region (Taguchi et al. 2000; Tatebe and Yasuda 2001), but note only relatively short altimeter records were used in these two studies, and most of the variability was associated with the annual cycle. HEOF analysis has also been used to summarize the output of ocean models (e.g., Hogg et al. 2005).

The present study aims to answer two main questions. 1) What are the dominant propagating modes of sea level variability in the Kuroshio Extension region? To answer this question HEOF analyses are performed on gridded weekly fields of observed sea level from 1993 to 2012 in two distinct frequency bands that cover time scales of months to decades. 2) What are the physical

causes of the dominant modes? We use a combination of theories (e.g., linear Rossby wave and thin-jet theory), a recent global ocean reanalysis, and statistical analysis of large-scale environmental indices to answer this question.

The structure of the paper is as follows. The observations, reanalysis datasets, and methods are reviewed in section 2. The variations of sea level and the latitude of the Kuroshio Extension jet are summarized in section 3. HEOF analysis of the altimeter observations is described in section 4, and the dominant modes are physically interpreted in section 5. Results are summarized and discussed in section 6.

2. Data and statistical methodology

Brief descriptions are now given for the observation and reanalysis datasets, and the main statistical techniques used to describe the observed and modeled sea level variability.

a. Observations and reanalyses

The sea level data were derived from altimeter observations from multiple satellite missions [Ocean Topography Experiment (TOPEX)/Poseidon (T/P), *European Remote Sensing Satellite* (*ERS*)*-1/2*, *Geosat*, and *Jason-1*]. The observations were processed by the Collecte Localisation Satellites (CLS) Space Oceanography Division of Toulouse, France, and distributed by Archiving, Validation, and Interpretation of Satellite Oceanographic data (AVISO) as part of the Environment and Climate European Union (EU) Enhanced Ocean Data Assimilation and Climate Prediction (ENACT) project supported by Centre National d'Études Spatiales (CNES). We used sea level anomaly and absolute dynamic topography fields initially published by AVISO in September 2010. The data were in the form of weekly, gridded fields with a grid spacing of 0.25°, from 1993 to 2012 inclusive. The annual and semiannual cycles have been removed from all gridpoint time series prior to analysis.

Surface wind fields for the North Pacific were obtained from the National Centers for Environmental Prediction (NCEP) Climate Forecast System Reanalysis (CFSR) (Saha et al. 2010). These fields were used to interpret results of the HEOF analysis of observed sea levels. The NCEP CFSR is a global, high-resolution, coupled atmosphere–ocean–land–sea ice system that has been used to generate reanalyses for the period 1979–2012 inclusive. Gridded 10-m wind fields, with a time step of 6 h and a grid spacing of 0.5°, were obtained. Winds were converted to stress using the drag formulation of Large and Pond (1981), averaged to daily values, and transformed into gridded fields of wind stress curl.

Three-dimensional current fields for the western North Pacific were obtained from the Global Ocean Reanalysis and Simulations (GLORYS), version 1 of the second reanalysis (GLORYS2V1), dataset made available by GLORYS and the EU-funded MyOcean project (Ferry et al. 2012). This reanalysis is based on an operational 3D ocean model with realistic forcing, bathymetry, baroclinicity, and so on. The data were in the form of monthly, gridded fields with a horizontal resolution of approximately 0.25° and 75 levels in the vertical. The data cover the period 1993–2009 inclusive. Observations from multiple sources, including altimeters and Argo vertical profilers, were assimilated. The GLORYS dataset has been shown to be highly skillful in reproducing observed variability of the main ocean variables (Ferry et al. 2012).

b. Hilbert empirical orthogonal function analysis

An overview is now provided of HEOF analysis and its relationship to conventional and frequency-dependent EOF analysis. We define several important parameters that are referenced later. Von Storch and Zwiers (1999) provide a more detailed discussion of most of the material presented in this subsection along with a historical review of the subject.

Let $\mathbf{X}_t = [X_{1t}, X_{2t}, \ldots, X_{pt}]'$ denote a real-valued random vector (where the square brackets indicate a vector) of length p. In the present context, one can think of the jth element of $\mathbf{X}_t$ as the sea level at spatial gridpoint j at time t. Assume $\{\ldots \mathbf{X}_{t-1}, \mathbf{X}_t, \mathbf{X}_{t+1}, \ldots\}$ is a stationary random process (where the curly brackets indicate a sequence) with zero mean and $p \times p$ covariance matrix at zero lag denoted by $\mathbf{\Sigma}_X$.

Conventional EOF analysis is based on an eigenanalysis of $\mathbf{\Sigma}_X$. The jth normalized eigenvalue $q_j = \lambda_j / \sum_k \lambda_k$ is the proportion of total variance (i.e., the trace of $\mathbf{\Sigma}_X$) accounted for by the jth mode. Frequency-dependent EOF analysis is a more general way of describing the modes of variability of $\mathbf{X}_t$. Let the cross spectrum between the jth and kth elements of the random process be denoted by $h_{jk}(\omega)$. The cross spectra associated with all possible pairs of elements (i.e., grid points) can be organized into a $p \times p$ spectral matrix, similar to a covariance matrix, with power spectra on the diagonal and cross spectra off the diagonal. Denote this cross-spectral matrix by $\mathbf{h}(\omega)$ and express it as $\mathbf{h}(\omega) = \mathbf{c}(\omega) - i\mathbf{q}(\omega)$, where $\mathbf{c}(\omega)$ is the matrix of cospectra and $\mathbf{q}(\omega)$ is the matrix of quadrature spectra. Frequency-dependent EOF is based on an eigenanalysis of $\mathbf{h}(\omega)$. It differs from conventional EOF analysis in two important ways: the eigenvectors can be complex and therefore describe propagating patterns in a single mode; and the eigenvectors and eigenvalues can vary with frequency. The proportion of

total power spectral density (i.e., the trace of $\mathbf{h}$) accounted for by the jth pattern is still q_j but it can now vary with frequency.

The relationship between conventional and frequency-dependent EOF analysis is evident in the following expression for the zero-lag covariance matrix in terms of the cospectral matrix:

$$\mathbf{\Sigma}_X = \int_{-\pi}^{\pi} \mathbf{c}(\omega)\, d\omega, \tag{1}$$

where we have use of the fact that $\mathbf{q}(\omega)$ is an odd function of ω. Thus, conventional EOF analysis is based on a "smoothed" cospectral matrix.

Hilbert EOF analysis is based on a "complexified," and possibly bandpass-filtered, version of the original process. Let $\sum_u g_u \mathbf{X}_{t-u}$ denote a filtered version of the process where $\{g_u\}$ is a sequence (indicated by the curly brackets) of filter weights. The spectral matrix of the filtered process at frequency ω is $|\Gamma(\omega)|^2 \mathbf{h}_X(\omega)|$, where $\Gamma(\omega) = \sum_u g_u e^{-i\omega u}$ is the transfer function of the filter. If $g_u = 2/\pi u$ for u odd, and zero otherwise, then $\Gamma(\omega) = -i\,\mathrm{sgn}(\omega)$. This particular filter corresponds to the Hilbert transform; it shifts the phase of each Fourier component of a time series by one-quarter of a cycle, but does not change the amplitude.

Denote the complexified version of the original multivariate process by $\mathbf{Z}_t = \mathbf{X}_t^B + i\,\mathbf{X}_t^{HB}$, where superscript B and H denote application of the bandpass filter and Hilbert transform, respectively. It is straightforward to show that the $p \times p$ covariance matrix of $\mathbf{Z}_t$ at zero lag is given by

$$\mathbf{\Sigma}_Z = 4 \int_0^{\pi} \Gamma_B^2(\omega) \mathbf{h}(\omega)\, d\omega, \tag{2}$$

where $\Gamma_B(\omega)$ is the real-valued transfer function of the (symmetric) bandpass filter. We will denote the band of this filter by $\omega_0 \pm \delta\omega$, where ω_0 determines the central frequency and $\delta\omega$ controls the width of the band. HEOF analysis is based on an eigenanalysis of $\mathbf{\Sigma}_Z$. If a narrow bandpass filter is used, HEOF analysis is approximately equivalent, up to a scale factor, to a frequency-dependent EOF analysis of $\mathbf{h}(\omega_0)$. Increasing the width of the filter's band (i.e., $\delta\omega$) means the HEOF analysis will search for propagating patterns that describe variability over a wider range of frequencies.

It is possible to reconstruct the original series using the first eigenvector of $\mathbf{\Sigma}_Z$ as follows:

$$\boldsymbol{X}_t^{\mathrm{recon}} = \Re[\alpha_1(t)\mathbf{e}_1], \tag{3}$$

where $\mathbf{e}_1 = \sqrt{\lambda_1}\tilde{\mathbf{e}}_1$ is the unit length eigenvector $\tilde{\mathbf{e}}_1$ scaled by the square root of the largest eigenvalue of $\mathbf{\Sigma}_Z$, and $\alpha_1(t) = (\tilde{\mathbf{e}}_1' \mathbf{Z}_t)/\sqrt{\lambda_1}$ is the (generally complex) time-varying amplitude. In the present study, the elements of $\mathbf{e}_1$ have the dimensions of observed sea level, and the amplitude $\alpha_1(t)$ is dimensionless and has unit variance.

The proportion of total variance of $\mathbf{\Sigma}_Z$ accounted for by the jth HEOF is given by $q_j(\omega_0)$. The results of HEOF analysis are thus strongly dependent on the width of the band of the filter applied to the original time series (i.e., $\delta\omega$). We discuss the selection of this parameter in section 4 and also provide plots of q_j as a function of ω_0 for sea levels observed in the Kuroshio Extension region. Appendix A illustrates, and discusses the limitations of, HEOF using results from a quasigeostrophic model.

3. Overview of variations in sea level and jet position

The first three moments of the weekly fields of observed sea level, sea level variability driven by large-scale changes in the observed wind stress curl, and variations in the path of the Kuroshio Extension jet, are now reviewed.

a. *First three moments of observed sea level variability*

The mean dynamic topography in the vicinity of the Kuroshio Extension jet (Fig. 1a) is dominated by two quasi-stationary meanders with crests near 144° and 150°E (e.g., Mizuno and White 1983). The generation mechanism of the meanders is controversial (Qiu 2002). They have been explained as lee waves linked to the Izu–Ogasawara Ridge (IO; Mizuno and White 1983) and also eddy-driven abyssal currents (Hurlburt et al. 1996). Recirculation gyres are also evident south of Japan and on the southern flank of the large meanders (Qiu and Chen 2005). A recirculation gyre on the northern flank has also been identified at middepth (Qiu et al. 2008). Downstream of the meanders, the jet bifurcates after crossing the Shatsky Rise (SR) with the main branch flowing slightly southward and broadening and the northeastward branch flowing along the subarctic front (Niiler et al. 2003).

The path of the mean Kuroshio Extension jet was estimated by mapping the speed of mean surface geostrophic flow and then associating the mean jet position with the local maximum in speed. We found that the jet path could be closely approximated by the 1-m contour of the mean dynamic topography (Fig. 1b), consistent with Qiu and Chen (2011).

The standard deviation of sea level is relatively high near the mean jet (Fig. 1b). The highest standard deviations occur west of the Shatsky Rise. A high-variance filament is also seen along the Kuril–Kamchatka Trench,

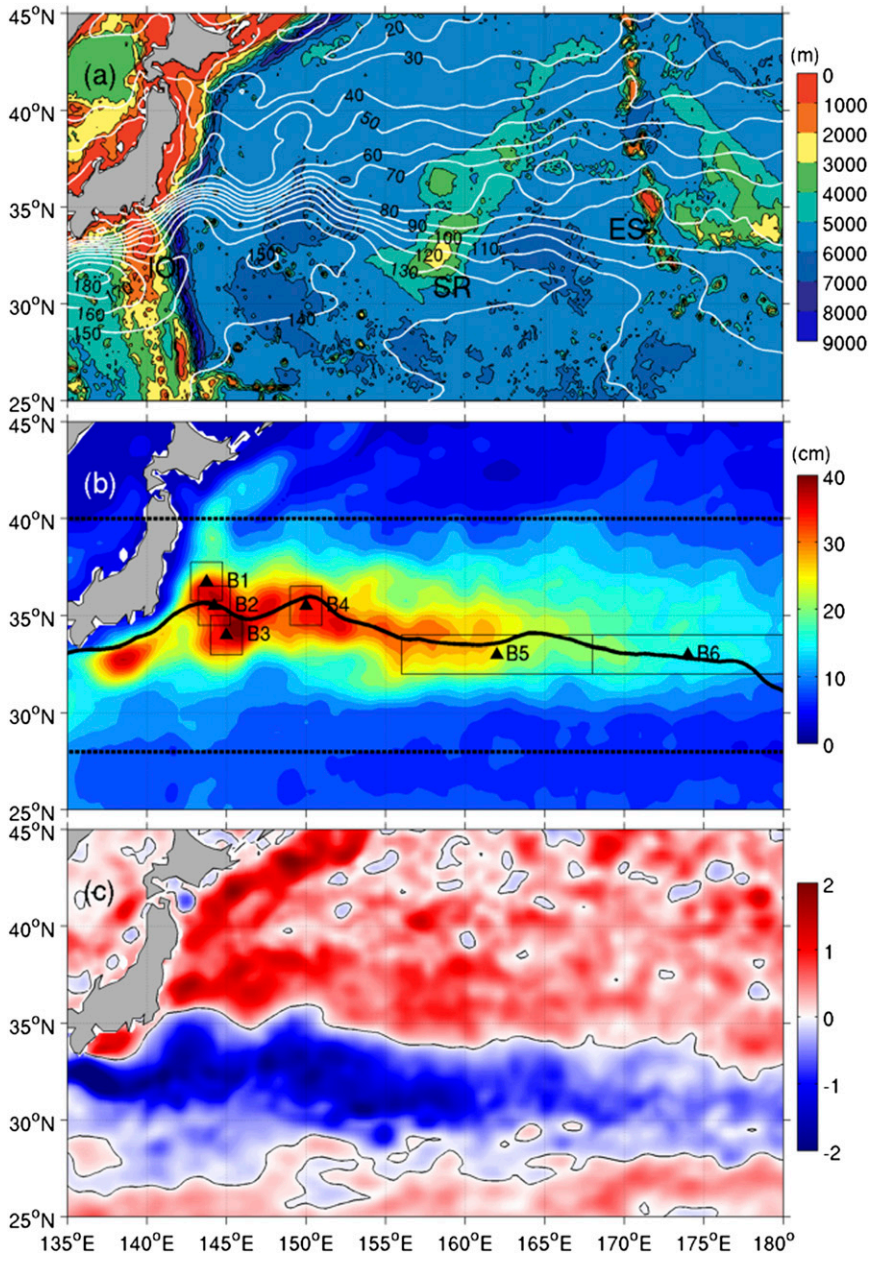

FIG. 1. Mean, std dev, and skewness of the weekly gridded sea level fields, 1993–2012. (a) Mean dynamic topography (white contours; cm) provided by AVISO. The bathymetry (colored; m) is also shown, along with labels for the following features: IO, SR, and ES. (b) Std dev (cm) calculated from individual gridpoint times series after removal of the annual and semiannual cycles. The black line is the long-term mean of the Kuroshio Extension jet based on the 1-m contour of the mean dynamic topography. The six boxes labeled from B1 to B6 define the averaging areas for the sea level time series plotted in Fig. 3. (c) Skewness calculated from the same data used for (b). The region defined by the dashed lines in (b), that is, 28°–40°N, 135°E–180°, is investigated in sections 4 and 5.

probably due to the high eddy activity in this region (Itoh and Yasuda 2010). Six boxes (from B1 to B6 in Fig. 1b) from the high-variance region have been chosen for further analysis.

The skewness of sea level (Fig. 1c) is consistent with the suggestion of Thompson and Demirov (2006) that the line of zero skewness can be used to identify the mean path and direction of unstable ocean jets. The

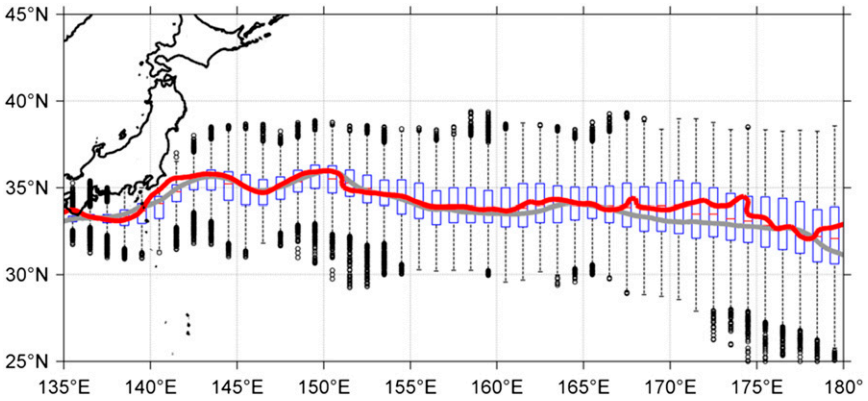

FIG. 2. Variability in the lat of the weekly Kuroshio Extension jet. Boxplots show the distribution of lat defined by the 1-m contour of the weekly sea level maps, 1993–2012. The thin red line inside the box shows the median, and the boundaries of the box show the first and third quartiles. The circles denote outliers (more than 1.5 times of the interquartile range from the edges of the boxes). The gray line is the long-term mean jet position (Fig. 1b), and the thick red line is the zero skewness contour (Fig. 1c).

more northerly zero skewness line (approximately 33°–36°N) in the Kuroshio Extension region coincides closely with the path of the mean jet with positive (negative) skewness to the left (right) of the flow direction. The agreement is particularly good to the west of about 165°E, where the latitudinal gradient in skewness is strongest (Fig. 2).

b. *Wind-driven sea level variability*

Following Qiu (2003), a linear model for nondispersive Rossby waves was used to investigate the effect of forcing by the large-scale wind stress curl. A first-order wave equation, forced by the daily curl field (section 2), was used to calculate the sea level for a given latitude. The model was spun up from rest, driven by the mean curl field, and then integrated from the eastern boundary over the period 1979–2012 using the observed time-varying curl. The hindcast sea level fields (henceforth η^{curl}) were averaged into weekly means to facilitate comparison with the altimeter data.

Time series of η^{curl} for six representative boxes (from B1 to B6; Fig. 1b) are shown as red lines in Fig. 3. Westward propagation is clearly evident, as expected. The amplitude of η^{curl} is on the order of 10 cm near the date line, increasing westward to about 20 cm in the meander region. These wind-driven predictions of sea level will be used to interpret the dominant modes of observed sea level.

c. *Variations in the path of the Kuroshio Extension jet*

The 1-m contour of the weekly sea level maps is now used to define the time-varying path of the Kuroshio Extension jet. The weekly latitude of the jet's position is summarized by the sequence of box plots (Fig. 2). Each box plot is based on all weekly latitudes observed within 1° of a given longitude. The medians (center lines of the boxes) generally coincide with the mean path position, consistent with the approximate symmetry of the histograms of the jet latitude for a given longitude. The spread of the meridional jet displacements increases downstream (e.g., Niiler et al. 2003); the interquartile range (covering 50% of the latitudes for a given box plot) increases from about 1° to 3° of latitude moving eastward from 142°E to 180°.

The meridional position of the Kuroshio Extension jet is known to change on time scales of months to decades (e.g., Qiu and Chen 2005). To visualize this variability over the period 1993–2012, we calculated the latitude ϕ of the 1-m sea level contour for each longitude λ and time t. To obtain a single latitude for each longitude and time, we averaged latitudes within 1° of a given central longitude for each weekly contour. The Hovmöller plot of ϕ against λ and t is dominated by the general westward-propagating signals of the jet axis and the two permanent meanders (Fig. 4a). Westward propagation is much clearer after removing the mean and annual and semiannual cycles from each ϕ time series (Fig. 4b).

The low-frequency variability of $\phi(\lambda, t)$ was obtained by applying a 1-yr running mean to the deseasonalized jet latitudes (Fig. 4c). A large, quasi-decadal oscillation is clearly visible with a more southerly jet around 1996 and 2007 and a more northerly jet around 2002 and 2012. Decadal oscillations in the position of the Kuroshio Extension jet have been noted in earlier studies (e.g., Qiu and Chen 2010; Sasaki et al. 2013). The decreasing amplitude of the meridional shifts as the signal propagates

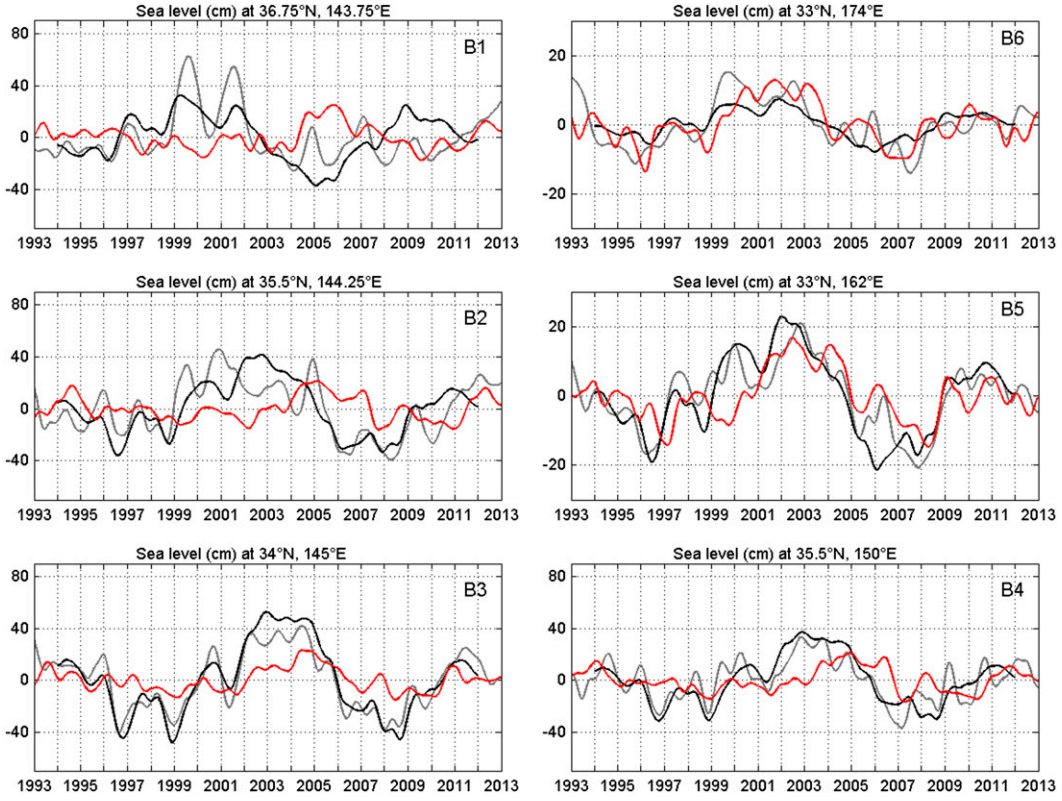

FIG. 3. Time variations of observed sea level η^{obs}, reconstructed sea level η^{recon}, and predictions from the linear, wind-driven model η^{curl}. The six locations are defined in Fig. 1b. Note the different y-axis scales. Observed weekly sea level, after removal of the mean and annual and semiannual cycles and spatial averaging over each box, is given in gray. Reconstructed sea level, calculated using (3), at the center of each box is given in black. Predictions by the linear, wind-driven model at the center of each box is shown in red. Both η^{obs} and η^{curl} have been deseasonalized and low-pass filtered with the cutoff of 350 days.

westward is consistent with Sasaki et al. (2013). The Hovmöller plot shows general westward propagation at low frequency, but it is difficult to estimate a reliable phase speed.

The high-frequency variability of jet latitude was obtained by subtracting Fig. 4c from Fig. 4b. Clear westward propagation is evident (Fig. 4d); the propagation speed was estimated to be 3.5 cm s^{-1} using the Radon transform (Deans 1983). The dominant period of the high-frequency variability was estimated to be 7–8 months, in agreement with Schmeits and Dijkstra (2002), who found a propagating mode with a similar period using multichannel singular spectrum analysis applied to altimeter data.

The instantaneous width of the Kuroshio Extension jet is on the order of 100 km, and the sea level drop across the jet is on the order of 1 m. As shown by Fig. 2, the latitudinal displacements often exceed 100 km, and so it is to be expected that much of the sea level variability in this region is due to shifts in the position of the jet (Sasaki et al. 2013). This expectation is consistent with the close alignment of the mean path of the jet and the line of zero skewness (Fig. 2).

4. HEOF analysis of the altimeter data

Observed sea level from the region defined by the dashed lines in Fig. 1b is now analyzed. To define the frequency bands for HEOF analysis, power spectra (not shown) were calculated for all gridpoint time series. Overall, the spectra were dominated by low-frequency variability in the vicinity of the jet. Apart from a slight elevation of energy at periods around 7 months, the spectra did not exhibit well-defined, spatially uniform spectral peaks over the study area. As noted by Barnett (1983), the absence of well-defined spectral peaks can complicate the application of HEOF analysis. We used the following approach to define the frequency bands for HEOF analysis.

a. Selecting the frequency bands for HEOF analysis

Each gridpoint time series of observed sea level was first bandpass filtered using a second-order Butterworth

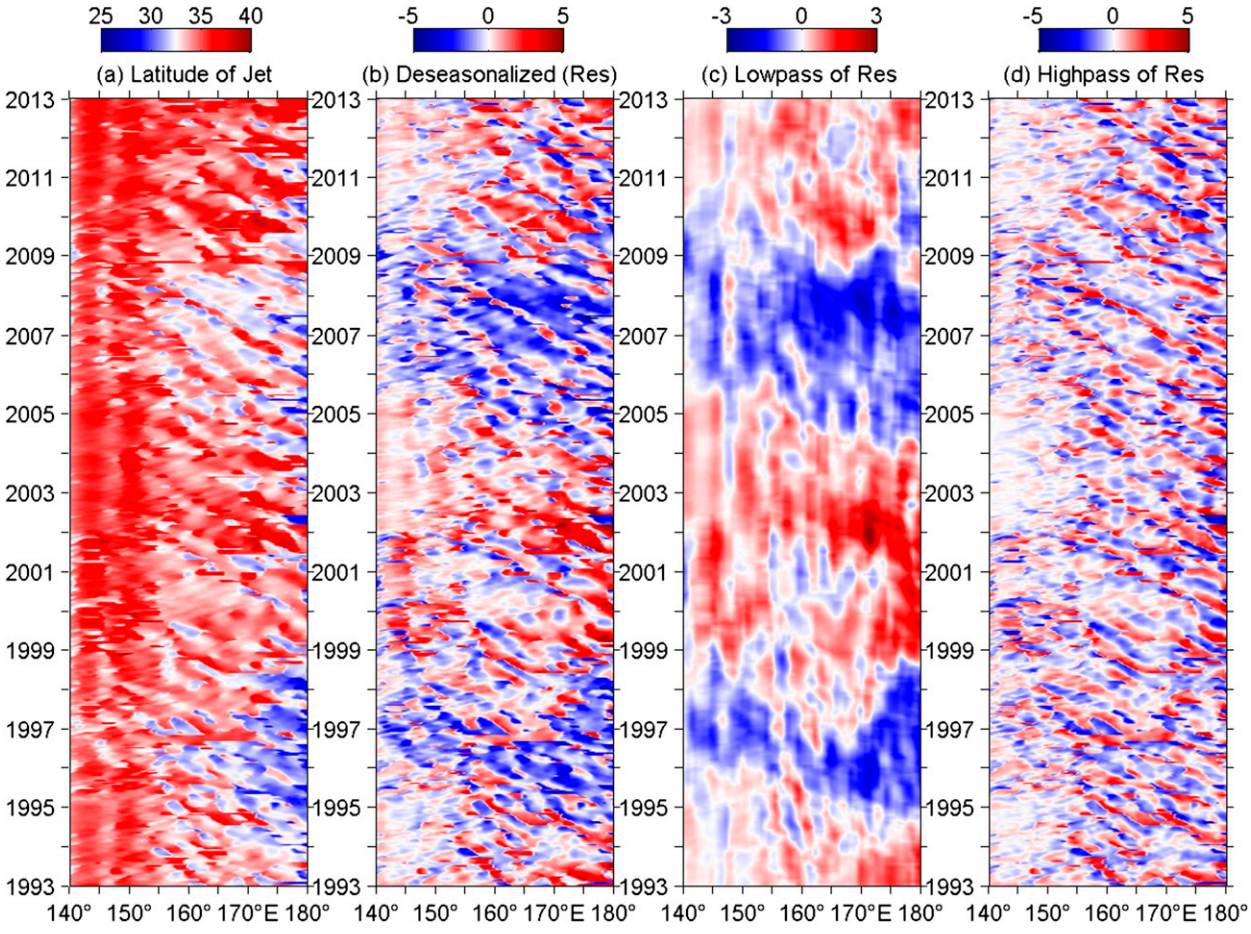

FIG. 4. Variation of the lat (°) of the Kuroshio Extension jet as a function of lon and time. (a) Weekly lat based on the 1-m contour. (b) Deseasonalized lat after removal of the mean, annual, and semiannual cycles from (a). (c) Low-frequency lat based on low-pass filtering in (b) to allow only variations with periods longer than 1 yr. (d) High-frequency lat given by the difference of (b) and (c).

filter with cutoff frequencies given by $\omega_0 \pm \delta\omega$. HEOF analyses were then performed on the filtered, Hilbert-transformed time series ($\mathbf{Z}_t$; see section 2) for different values of ω_0. The choice of $\delta\omega$ is subjective in the absence of a well-defined spectral peak (e.g., Barnett 1983). Based on sensitivity studies with different $\delta\omega$, we finally chose $\delta\omega = 1/700$ cycles per day. This choice is a compromise between a small value of $\delta\omega$ needed to resolve rapid changes of the HEOFs with frequency and a large value needed for statistically stable results (specifically high degrees of freedom for reliable estimation of $\mathbf{\Sigma}_Z$).

A statistical summary of the HEOF analyses as a function of frequency is provided in Fig. 5. The triangles in Fig. 5 (top) show the total variance of $\mathbf{Z}_t$ for all grid points (i.e., the trace of $\mathbf{\Sigma}_Z$) increases with decreasing frequency. A slight elevation of total variance is seen at a period of about 7 months. The circles show the largest eigenvalue of the covariance matrix of $\mathbf{Z}_t$ also increases with decreasing frequency. The proportion of total variance accounted by the first HEOF [i.e., $q_1(\omega_0)$; Fig. 5, bottom] also increases with decreasing frequency and has a local maximum centered on a period of about 7 months. Based on the plots of $\mathbf{\Sigma}_Z$ and $q_1(\omega_0)$, we chose two frequency bands for further study: a ''low frequency'' band, corresponding to periods longer than 350 days, and a ''high frequency'' band corresponding to periods between 140 and 350 days (see vertical dashed lines in Fig. 5, bottom).

Sensitivity studies were performed on the effect of changing the widths of the two chosen frequency bands (i.e., $\delta\omega$). For example, we found that halving the width of both bands had little effect on $\mathbf{e}_1^{\text{low}}$ and $\mathbf{e}_1^{\text{high}}$. We also checked the sensitivity of $\mathbf{e}_1^{\text{high}}$ to changes in the longitudinal limit of the study region: changing the extent from 135°E–180° to 150°E–180°, and 135°–165°E, caused no significant changes in $\mathbf{e}_1^{\text{high}}$. We therefore conclude that the following description of $\mathbf{e}_1^{\text{low}}$ and $\mathbf{e}_1^{\text{high}}$ will still

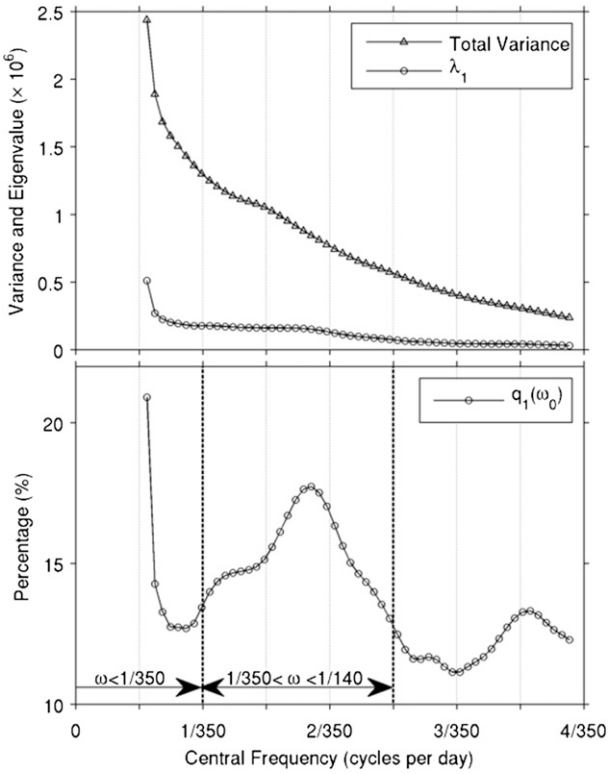

FIG. 5. Statistical summary of the HEOF analysis of observed sea level for the Kuroshio Extension region. Each time series was bandpass filtered using a half-width of $\delta\omega = 1/700$ cycles per day. (top) The total variance of $\mathbf{\Sigma}_Z(\omega_0)$ and its largest eigenvalue. (bottom) The normalized eigenvalues $[q_1(\omega_0)$, see section 2]. The vertical dashed lines define the low- and high-frequency bands discussed in section 4.

apply given reasonable changes in the width of the chosen frequency bands and the longitudinal extent of the study region.

b. High frequency

The dominant high-frequency mode ($\mathbf{e}_1^{\text{high}}$) accounts for 15% of the total high-frequency variance. The highest amplitudes of this mode ($|\mathbf{e}_1^{\text{high}}|$; see Fig. 6a) occur in the vicinity of the Shatsky Rise and Emperor Seamounts (ES), where the typical changes of sea level are about 25 and 10 cm, respectively. The corresponding phase map (Fig. 6b) indicates general westward propagation over much of the area (Fig. 6b). Wang et al. (1998a) also presented an intra-annual complex EOF (their Fig. 10) with a structure similar to $\mathbf{e}_1^{\text{high}}$ near the Shatsky Rise, but no clear large amplitudes were found in the vicinity of the Emperor Seamounts. The length of the time series analyzed by Wang et al. (1998a) was much shorter (4.2 yr) than the time series analyzed here (20 yr). Plots (not shown) of the time series and power spectrum of α_1^{high} indicate that the dominant period of this mode is approximately 7 months. The spacing of the phase contours in the large-amplitude areas implies a phase speed of about 3 cm s^{-1}.

To check the robustness of $\mathbf{e}_1^{\text{high}}$, an HEOF analysis was also performed on the high-frequency sea level for the entire North Pacific. The spatial structure of dominant HEOF (not shown) was found to be similar to Fig. 6 in the overlap region; both modes indicate general westward propagation and higher amplitudes in the vicinity of the Shatsky Rise and Emperor Seamounts. The HEOF for the entire North Pacific has amplitudes typically less than 1 cm east of the date line.

c. Low frequency

Before describing the low-frequency HEOF, we examine observed sea level variability averaged over each of the six boxes (from B1 to B6) in the high-variance region (Fig. 1b). Time series plots (Fig. 3, gray lines) indicate westward propagation from B6 to B3. This is confirmed by the complex correlations of observed sea level from different locations (Table 1). Taking B6 as the base station, the magnitude of the correlations with B6 is everywhere above 0.6 (significant at the 5% level; see appendix B), and the phase indicates westward-propagating signals with an approximately 70° lag at B3 (corresponding to a lag of about 2 yr assuming a decadal period). Figure 3 also indicates that the amplitude almost doubles from B6 to B3. Taking B1 as the base station, Fig. 3 and Table 1 suggest that low-frequency variations at B1 lead changes at B3 by about 3 yr. Also, sea level changes at B1 lead changes at B6 by about 6 months based on the phase lag in Table 1 and the cross correlation between the two time series (not shown).

The dominant low-frequency mode ($\mathbf{e}_1^{\text{low}}$) accounts for 27% of the total low-frequency variance. The highest values of $|\mathbf{e}_1^{\text{low}}|$ occur near the mean path of the Kuroshio Extension jet and generally increase westward, reaching about 40 cm in the meander region (Fig. 7a). A similar pattern was found in the dominant low-frequency HEOF of the quasigeostrophic model described in appendix A. The phase map (Fig. 7b) indicates general westward propagation along the mean path, between about 155°E and 180°. In the meander region, the phase contours are approximately aligned with the path of the mean jet and indicate southward propagation across the jet. The time-varying amplitude α_1^{low} has a dominant period of about 10 yr (Fig. 8).

There is generally good agreement between observed and reconstructed low-frequency sea levels at all six locations (black and gray lines in Fig. 3; Table 1), consistent with the high proportion of variance captured by $\mathbf{e}_1^{\text{low}}$ along the jet and in the meander region. The

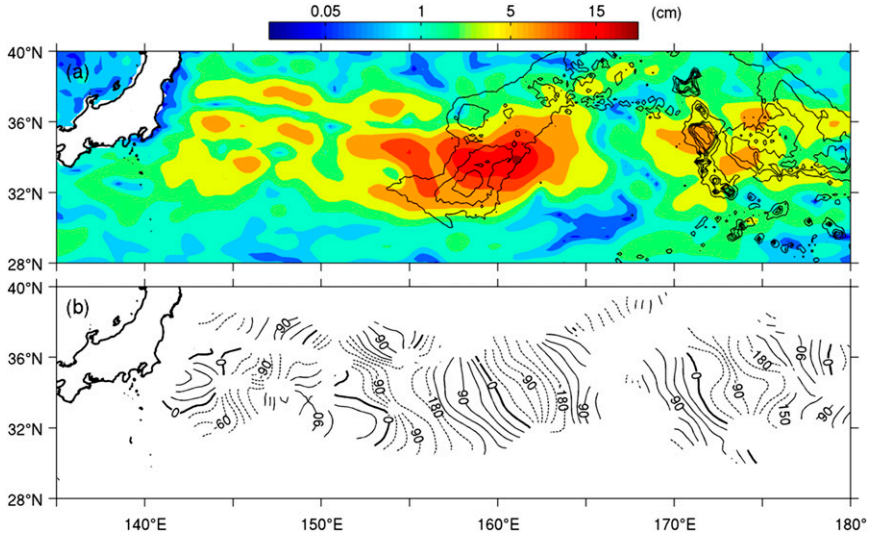

FIG. 6. Dominant mode of observed high-frequency sea level ($\mathbf{e}_1^{\text{high}}$). (a) The amplitude and (b) phase. The phase contour interval is 30°. The zero phase contour is shown in heavy line; contours from −180° to −30° and from 30° to 150° are shown by thin dashed and solid lines, respectively. Phase contours are only plotted for regions where the magnitude of $\mathbf{e}_1^{\text{high}}$ exceeds 3 cm. Selected depth contours (1000–5000 m with 1000-m interval; black lines in Fig. 6a) have been added to the amplitude map to show the SR and ES. A nonlinear color scale is used in (a).

magnitudes of the complex correlations between η^{obs} and η^{recon} range from 0.59 to 0.94; most of the phase lags are less than 10°. The Hovmöller plot (Fig. 9) of η^{recon} along the section defined in Fig. 7 indicates westward propagation between 180° and 150°E (sections S3 and S4), with the amplitude increasing to the west. In the meander region, the variations of η^{recon} reach almost 0.5 m. Changes in η^{recon} along S1 also confirm sea level north of the jet leading by about 3 yr.

5. Physical interpretation of the dominant modes

The modes described in the previous section are interpreted in this section using linear Rossby wave and thin-jet theory and output from a recent ocean reanalysis.

a. High frequency

The Hovmöller diagram presented in Fig. 10 (top) shows high-frequency sea level variability, averaged between 31° and 37°N, as a function of time and longitude. This zonal section extends from the meander region to the eastern boundary of the North Pacific. (One reason for introducing this new section was to check if the sea level along the eastern boundary was generating Rossby waves as seen in the quasigeostrophic model simulations described in appendix A.) Westward-propagating signals with an amplitude on the order of 15 cm are evident west of the date line. Westward-propagating signals can also be seen in the eastern part of the basin, but they are weaker (less than 2 cm and spatially uniform) and lack coherency as they travel from the coast to the date line. Based on these results, it is difficult to argue that the high-frequency signals are forced by large-scale sea level changes along the eastern boundary.

To further check if sea level variability along the eastern boundary has a significant impact on the structure of $\mathbf{e}_1^{\text{high}}$, an additional HEOF analysis was performed on the high-frequency sea level for the eastern North Pacific (from 20° to 60°N, east of 160°W). The

TABLE 1. Amplitude and phase (°) of the complex correlation of η^{obs}, η^{recon}, η^{curl}, and the PDO. The locations of the sea levels are defined by the boxes in Fig. 1b. All series except η^{recon} were low-pass filtered (350-day cutoff) first. Correlations that are significantly different from zero at the 5% (10%) level are shown in boldface (italics).

	η^{obs}					
Amplitude	B1	B2	B3	B4	B5	B6
η^{obs} (B6)	**0.61**	**0.61**	**0.66**	**0.61**	**0.75**	**1**
η^{obs} (B1)	**1**	**0.60**	**0.49**	*0.42*	0.39	**0.61**
η^{recon}	**0.59**	**0.70**	**0.94**	**0.82**	**0.87**	**0.78**
η^{curl}	0.18	*0.48*	**0.80**	**0.70**	**0.75**	**0.75**
PDO	**0.55**	*0.41*	*0.42*	0.31	*0.43*	**0.52**
Phase (°)						
η^{obs} (B6)	22	−20	−69	−44	−21	0
η^{obs} (B1)	0	−23	−112	−91	−51	−22
η^{recon}	13	−4	−3	−7	8	8
η^{curl}	150	−84	−35	−57	−26	−20
PDO	−167	−106	−64	−92	−78	−132

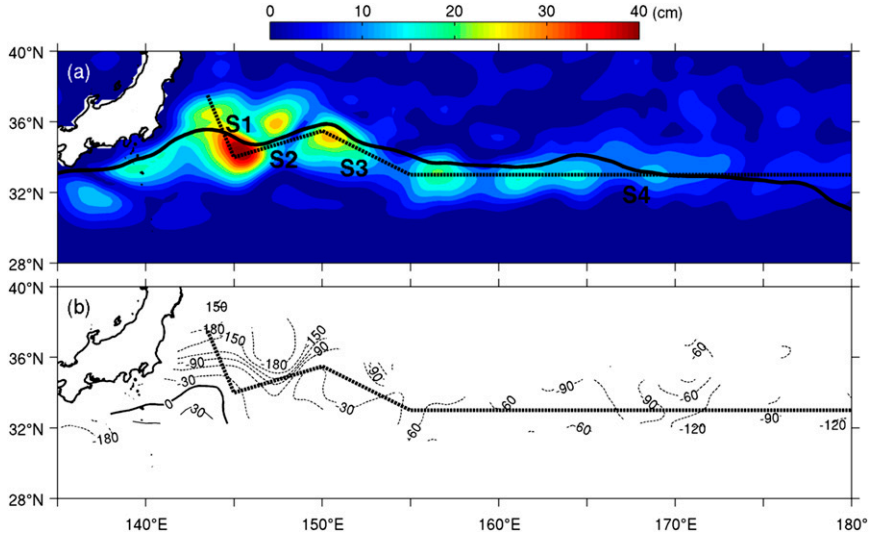

FIG. 7. Dominant mode of observed low-frequency sea level ($\mathbf{e}_1^{\text{low}}$). Similar format to Fig. 6. The heavy solid line in (a) is the mean path of the Kuroshio Extension jet (Fig. 1b). Phase contours are only plotted for regions where the magnitude of $\mathbf{e}_1^{\text{low}}$ exceeds 6 cm. The heavy dashed line (and labels S1–S4) denotes the sections used for Fig. 9 (described in greater detail below).

dominant mode (not shown) has the largest amplitudes (about 4 cm) close to the coast of the Gulf of Alaska; away from the coast, the amplitude was typically less than 2 cm. Again, no evidence of coherent westward-propagating signals originating at the eastern boundary was found. We conclude that high-frequency sea level variability along the eastern boundary is unlikely to be a major driver of Rossby waves in the Kuroshio Extension region. This is consistent with Fu and Qiu (2002) who reported that boundary-driven sea level variability had a limited offshore influence.

It is interesting to note that the standard deviation of the high-frequency variability correlates well with the underlying bathymetry (Fig. 10); sea level signals are clearly strongest in the vicinity of the Emperor Seamounts (near the date line) and Shatsky Rise (near 160°E) and then decrease to the west. This leads us to speculate that the dominant high-frequency HEOF is the result of Rossby waves generated by the Kuroshio Extension jet's interaction with the Shatsky Rise and Emperor Seamounts. Support for this speculation comes from Greene (2010), who

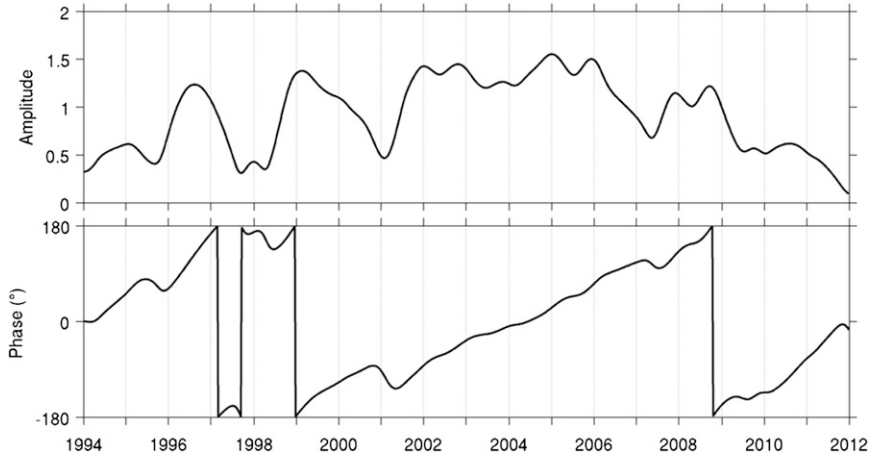

FIG. 8. Time-varying amplitude of the dominant mode of observed low-frequency sea level variability $\alpha_1^{\text{low}}(t)$. (top) The amplitude (nondimensional) and (bottom) the phase (°). The time series covers the period 1994–2011 to remove end effects of the low-pass filter.

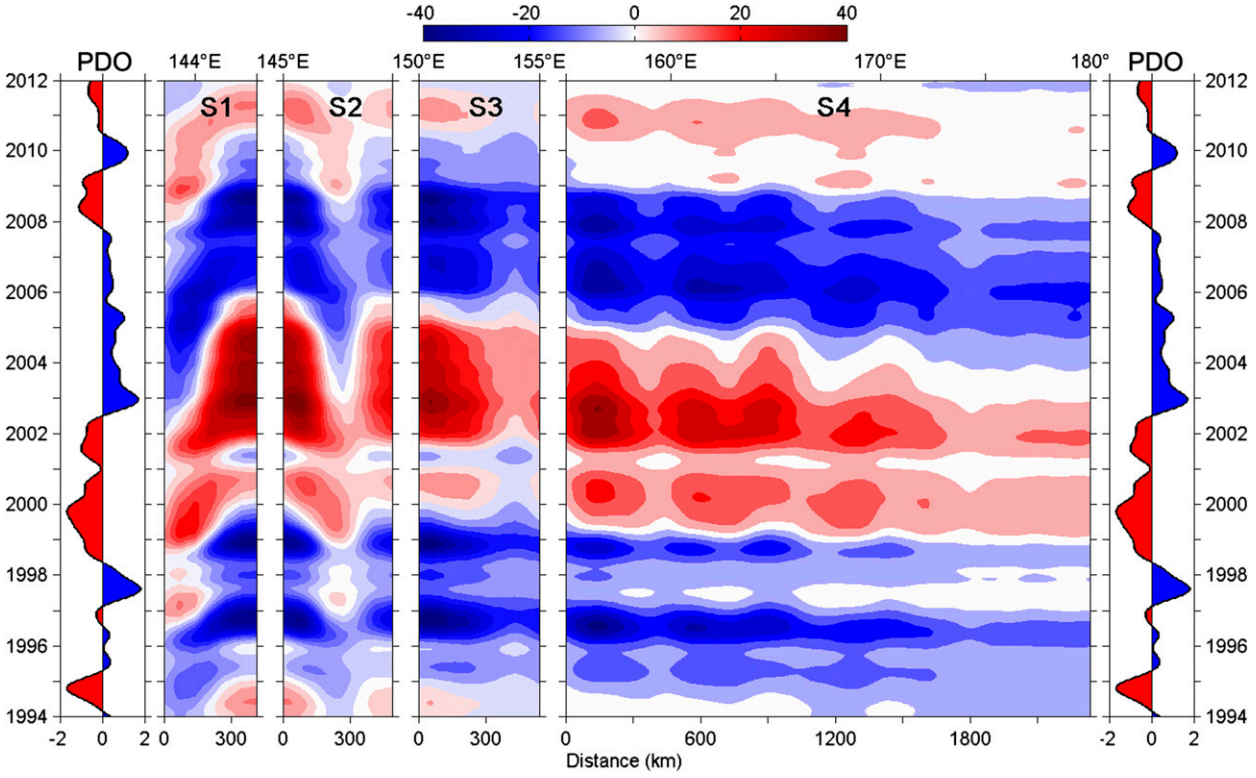

FIG. 9. Hovmöller plot of reconstructed sea level [cm; see (3)] along sections S1–S4 defined by the dashed lines in Fig. 7. The PDO index is shown in the leftmost and rightmost panels. (The index was obtained from http://jisao.washington.edu/pdo/PDO.latest). To facilitate comparison with the low-frequency sea levels, the index was interpolated to weekly values, detrended, deseasonalized, and low-pass filtered (with a cutoff of 350 days).

recently concluded that high-frequency (periods of 30–60 days) topographic Rossby waves (Rhines and Bretherton 1973) observed in the Kuroshio Extension originate from the Shatsky Rise. The conclusion was based on a combination of observations, collected during the Kuroshio Extension System Study in the meander region and simulations by the Ocean General Circulation Model for the Earth Simulator (OFES) that extended the analysis eastward to include the Shatsky Rise. Qiu and Chen (2010) also reported that low-frequency variations in the position of the Kuroshio Extension jet in the vicinity of the Shatsky Rise could trigger perturbations that subsequently propagate westward.

b. *Low frequency*

Low-frequency sea level variability along the mean path of the jet is first interpreted by comparing η^{obs} with η^{curl}, and an index of large-scale environmental conditions over the North Pacific, specifically the Pacific decadal oscillation (PDO). Variations across the jet in the meander region are then investigated using GLORYS.

1) JET-TRAPPED ROSSBY WAVES

At the easternmost box (B6), there is good agreement between η^{obs} and η^{curl} in terms of both amplitude and timing (Fig. 3, gray and red lines). The magnitude of the complex correlation is 0.75 with a phase lag of −20° (Table 1). This good agreement is consistent with previous studies (e.g., Qiu 2003). The correlation between η^{obs} and η^{curl} remains high from B5 to B3, but η^{curl} increasingly underestimates the amplitude of η^{obs} moving westward, consistent with the results of Sasaki et al. (2013). Although the linear Rossby wave model provides an accurate prediction of sea level at B6, it cannot explain the observed variations of sea level, or η^{recon}, from B5 to B3. The phase of the complex correlation (Table 1) also increases westward, indicating that η^{curl} progressively lags η^{obs}. This is likely due to errors in the phase speed used to calculate η^{curl}. Note that Sasaki et al. (2013) estimated a phase speed that was closer to 5 cm s^{-1} at this latitude.

We also related η^{obs} to the PDO. We chose this index for two reasons. First, it has been shown in many studies that there is a relationship between the PDO and sea

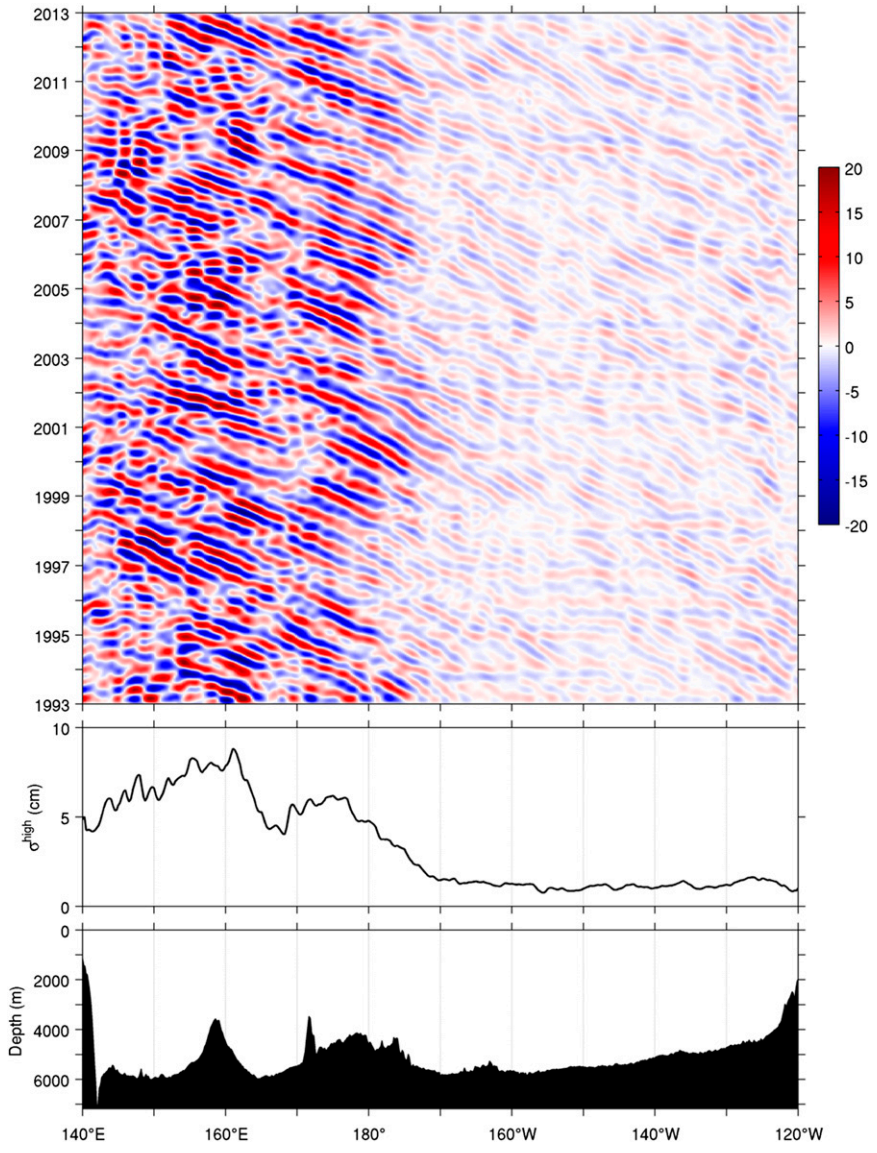

FIG. 10. Observed high-frequency sea level variability across the North Pacific. (top) Hovmöller plot of high-frequency sea level (cm) as a function of lon (from 140°E to 120°W) and time (from 1993 to 2012). The sea level data have been deseasonalized and bandpass filtered with cutoff periods of 140 and 350 days. Sea level at each lon was averaged meridionally between 31° and 37°N to match the region where the amplitude of the dominant high-frequency HEOF is largest. (middle) Std dev of the high-frequency sea level. (bottom) Bathymetry, also averaged meridionally between 31° and 37°N.

level in the Kuroshio Extension region (e.g., Andres et al. 2009; Qiu and Chen 2010). Second, the PDO is known to be a proxy for the large-scale wind field (e.g., Andres et al. 2011). To quantify the relationship between the PDO and wind stress curl, we formed composite maps of curl anomaly conditioned on the low-frequency PDO. The composite curl anomaly maps at anomalously high and low PDO values (not shown) were quite similar except for a reversed sign. The curl anomaly maps for positive PDO resemble the mean field. This implies that a positive (negative) PDO corresponds to stronger (weaker) curl forcing.

The low-frequency PDO index has a clear negative correlation with the low-frequency sea level at the date line and north of the jet (Fig. 9). Closer inspection of Fig. 9, cross correlation of the PDO with η^{obs} and η^{recon} (not shown), and the complex correlations between the PDO and η^{obs} from B1 to B6 (Table 1) all indicate that the

PDO leads sea level by about 1 yr at the date line and about half a year north of the jet.

Sasaki et al. (2013) recently used thin-jet theory to explain their EOF analysis of sea level variability in the Kuroshio Extension region. They reached several conclusions that are consistent with the structure of $\mathbf{e}_1^{\text{low}}$. (i) The phase speed of west-propagating anomalies in jet position is about 5 cm s^{-1}. The phase map of $\mathbf{e}_1^{\text{low}}$ (Fig. 7b) gives a similar propagation speed based on fitting the phase changes with the distance along sections S3 and S4. Furthermore, the lag of sea level at B3 relative to B6 (Table 1) is 70°, which corresponds to a time lag of about 2 yr and a phase speed of about 5 cm s^{-1}. (ii) Anomalies propagate along the mean path of the jet, rather than a line of constant latitude, as predicted by linear Rossby wave theory, and will be trapped close to the jet. This is consistent with the map of $|\mathbf{e}_1^{\text{low}}|$ (Fig. 7a) that shows elevated amplitudes along the path of the mean jet. (iii) The amplitude of sea level changes caused by jet displacements vary with the mean sea level drop across the jet. Sasaki et al. (2013) also showed that the mean sea level drop across the jet, with respect to the instantaneous jet position, increases from about 30 cm at the date line to 90 cm at 145°E (their Fig. 10b). These values are in reasonable agreement with ranges in η^{recon} from B6 to B3 (Fig. 3); the ranges of η^{recon} are 15, 45, 70, and 100 cm, respectively. The westward increase in amplitude is also consistent with the map of $|\mathbf{e}_1^{\text{low}}|$ shown in Fig. 7a.

Based on the above discussion, we conclude that the structure of $\mathbf{e}_1^{\text{low}}$ along the mean path of the jet is due primarily to baroclinic, jet-trapped Rossby waves forced by the large-scale wind stress curl east of the date line.

2) SEA LEVEL ANTICIPATION NORTH OF THE JET

At the three locations in the permanent meander region straddling the jet (from B1 to B3), the changes of η^{curl} are too small, and large scale, to explain η^{obs}. To a first approximation, there is a 180° phase shift across the jet that implies that high (low) sea levels south of the jet are associated with steeper (shallower) sea level slopes across the jet and thus faster (slower) jet speeds. This has led several authors (e.g., Taguchi et al. 2005; Sasaki et al. 2013) to conclude that westward-propagating, positive (negative) sea level anomalies are associated with the strengthening (weakening) of the upstream jet after they reach the coast of Japan.

Closer examination of the phase map of $\mathbf{e}_1^{\text{low}}$ (Fig. 7b), the Hovmöller plot of η^{recon} along section S1 (Fig. 9), and time series of η^{obs} (Fig. 3; Table 1) all suggest that decadal changes of sea level at B1, north of the jet, lead sea level at B3, south of the jet, by about 3 yr.

A possible explanation for this anticipation is the fast barotropic response of the western boundary currents to changes in the large-scale wind forcing. An increase in the PDO is associated with a contemporaneous increase in the wind curl over the North Pacific (see above), and this will increase the barotropic transport of the western boundary currents within about 1 month (e.g., Gill 1982). With this in mind we used the GLORYS dataset (see section 2) to estimate the time-varying transport (U, V) of the Kuroshio system. Note that this approach takes into account the effect of variations in bathymetry on the barotropic response. (The transport was calculated by vertically integrating the depth-varying flow for each grid point over the complete water column.)

The mean transport in the study region is complicated (Fig. 11a). Large integrated transports [tens of Sverdrups (Sv); 1 Sv $\equiv 10^6$ m^3 s^{-1}] can be seen flowing along the trench near the western boundary, in the meander region, and upstream in the East China Sea. The standard deviation of the monthly GLORYS transports ($\sqrt{\sigma_U^2 + \sigma_V^2}$; Fig. 11b) also indicates enhanced variability along the trench, in the meander region, and in the deep basin between the Shatsky Rise and Emperor Seamounts. Transport variability is weaker on the west side of the Izu–Ogasawara Ridge, suggesting shielding by this bathymetric feature.

The mean and standard deviation maps both show that transport is highly variable in the western North Pacific. Our attempts to pick a single representative section to define the overall transport were unsuccessful; transports calculated through adjacent sections decorrelated quickly with increasing separation between sections. To obtain a single index of western boundary transport variability we performed a vector EOF (VEOF) analysis on the deseasonalized monthly U and V time series. To focus on the western boundary region, and omit the large transport variability in the meander region, we only used U and V from grid points in the vicinity of the trench. (The selected points have water depths greater than 6000 m and are shown in Fig. 12a). The first VEOF has two branches flowing along the trench in different directions north and south of the separation point (red arrows in Fig. 12a). The corresponding principal component (α_1^{trans}; red curve in Fig. 12b) is dominated by low-frequency variability that implies transport changes of about ±10 Sv.

The transport index (α_1^{trans}) is coherent at low frequency with both the PDO and sea level north of the jet (η^{B1}; Fig. 12b). The phase lag between α_1^{trans} and both the PDO and η^{B1} is small. Our interpretation of these results is that time variation of the curl field, indexed by the PDO, drives a barotropic response of the ocean

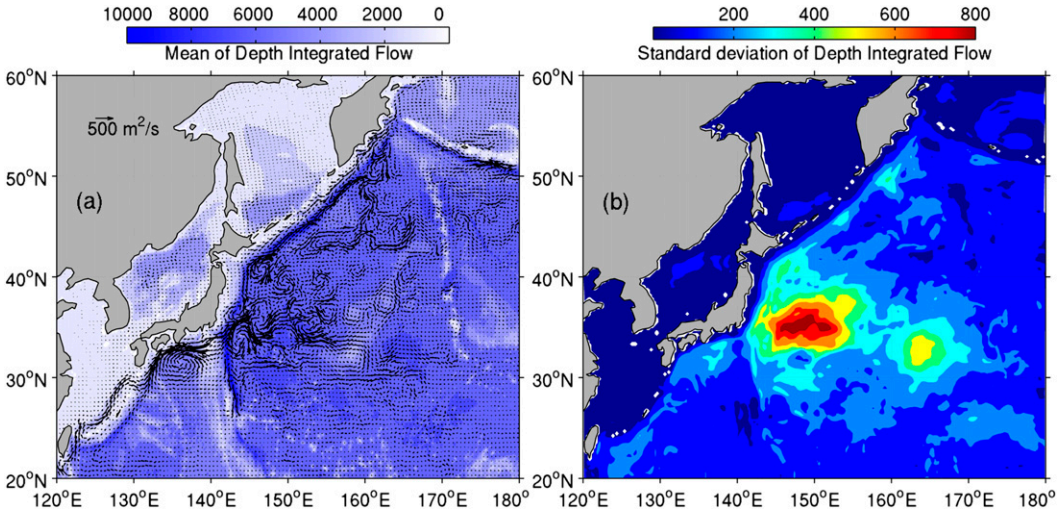

FIG. 11. Transport in the western North Pacific based on GLORYS, 1993–2009. (a) Mean and (b) std dev ($m^2 s^{-1}$). The blue shading in (a) shows the bathymetry (m). The scale for the mean transport is shown by the arrow in the top-left corner of (a).

leading to rapid, large-scale changes in the western boundary transport. These variations of transport then drive circulation changes in the meander region, leading to changes in η^{B1}. To test this interpretation, we calculated the streamfunction from GLORYS and then regressed each gridpoint time series onto α_1^{trans} (black contours, Fig. 12a). The regression coefficient pattern has positive (negative) values to the north (south) of the jet. This means an increase (decrease) of α_1^{trans} is associated with (i) a diverging (converging) transport along the western boundary, (ii) an anticyclonic (cyclonic) circulation north of the jet, and (iii) a positive (negative) sea level anomaly at B1. The above results are consistent with our speculation that changes in western boundary transport (due to a barotropic response to large-scale wind forcing) are associated with changes in sea level, and circulation, in the meander region.

We conclude this section with a summary plot (Fig. 13) of annual-mean sea level anomalies from the Kuroshio Extension region, 1993–2012. The westward propagation of jet-trapped Rossby waves and the anticipation of sea level north of the jet are evident. To illustrate the anticipation, consider the period 1998–2007 when the PDO undergoes a particularly well-defined decadal cycle. In 1998, the PDO becomes negative, indicating that the wind curl pattern over the North Pacific is weaker than usual. A positive sea level anomaly starts to appear north of the jet, close to B1. As this anomaly intensifies over the following year, a positive sea level anomaly appears near the date line and propagates westward as a jet-trapped Rossby wave. This propagating signal reaches the meander region, close to B3, by about 2002. In the same year, a negative sea level anomaly begins to form north of the jet, and the cycle continues.

6. Summary and discussion

Hilbert empirical orthogonal function analysis has been used to provide a low-dimensional, frequency-dependent description of observed sea level variability in the Kuroshio Extension region on time scales of months to decades. The observations cover the period from 1993 to 2012 inclusive. A linear, nondispersive Rossby wave model, the recent thin-jet theory of Sasaki et al. (2013), empirical relationships with the PDO, and results from a recent global ocean reanalysis were used to physically explain the dominant modes.

The observed variability of the latitude of the Kuroshio Extension jet was first summarized in a longitude–time plot. Latitudinal shifts on the order of 3° on decadal time scales, and on the order of 5° on time scales of 7–8 months, were observed to propagate westward. The amplitude of the decadal shifts were observed to decrease as the signals propagated westward, consistent with the study of Sasaki et al. (2013). Latitudinal shifts of jet position on both time scales had length scales on the order of 3000 km.

The dominant high-frequency HEOF of observed sea level (periods between 140 and 350 days) has the largest amplitudes in the vicinity of the Shatsky Rise (about 25 cm) and Emperor Seamounts (about 10 cm). The corresponding phase map shows westward propagation. Based on a Hovmöller plot of high-frequency sea level variability along a zonal band extending from the meander region to the coast of North America, and

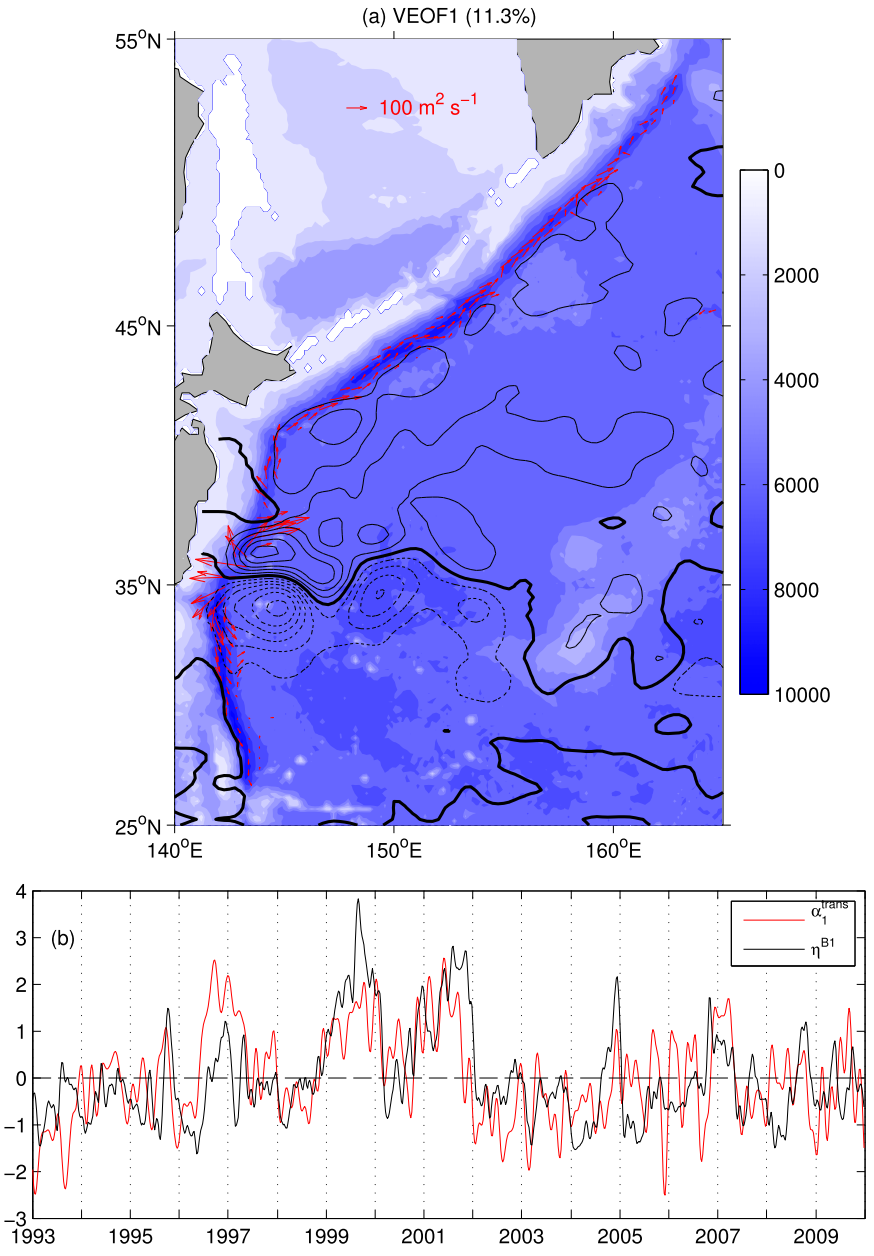

FIG. 12. VEOF analysis of the western boundary transport from GLORYS, 1993–2009. (a) The dominant eigenvector (red arrows). (b) The first principal component (red; α_1^{trans}) and normalized sea level at B1(black; for location see Fig. 1b). The black contours in (a) show the regression coefficient from the regression of streamfunction (calculated from the GLORYS transports) on α_1^{trans}. The contour interval is 5, with zero contours shown by heavy lines and positive (negative) contour values shown by thin solid (dashed) lines. Regression coefficients in the marginal seas have been masked out.

additional HEOF analysis of the eastern North Pacific, we conclude that $\mathbf{e}_1^{\text{high}}$ is not forced by sea level variation along the eastern boundary. The close correspondence between sea level variance and bathymetry leads us to speculate that $\mathbf{e}_1^{\text{high}}$ is associated with Rossby waves generated by the Kuroshio Extension jet interacting with the Shatsky Rise and Emperor Seamounts.

Lin et al. (2008) recently showed that the peak in the power spectra of observed sea level from the North Pacific matched closely the critical frequency for the existence of Rossby waves ($\omega_{\max} = \beta a/2$, where a is the internal Rossby radius; Gill 1982). They explained this result in terms of an amplified response of the ocean to external forcing at the frequency where the group

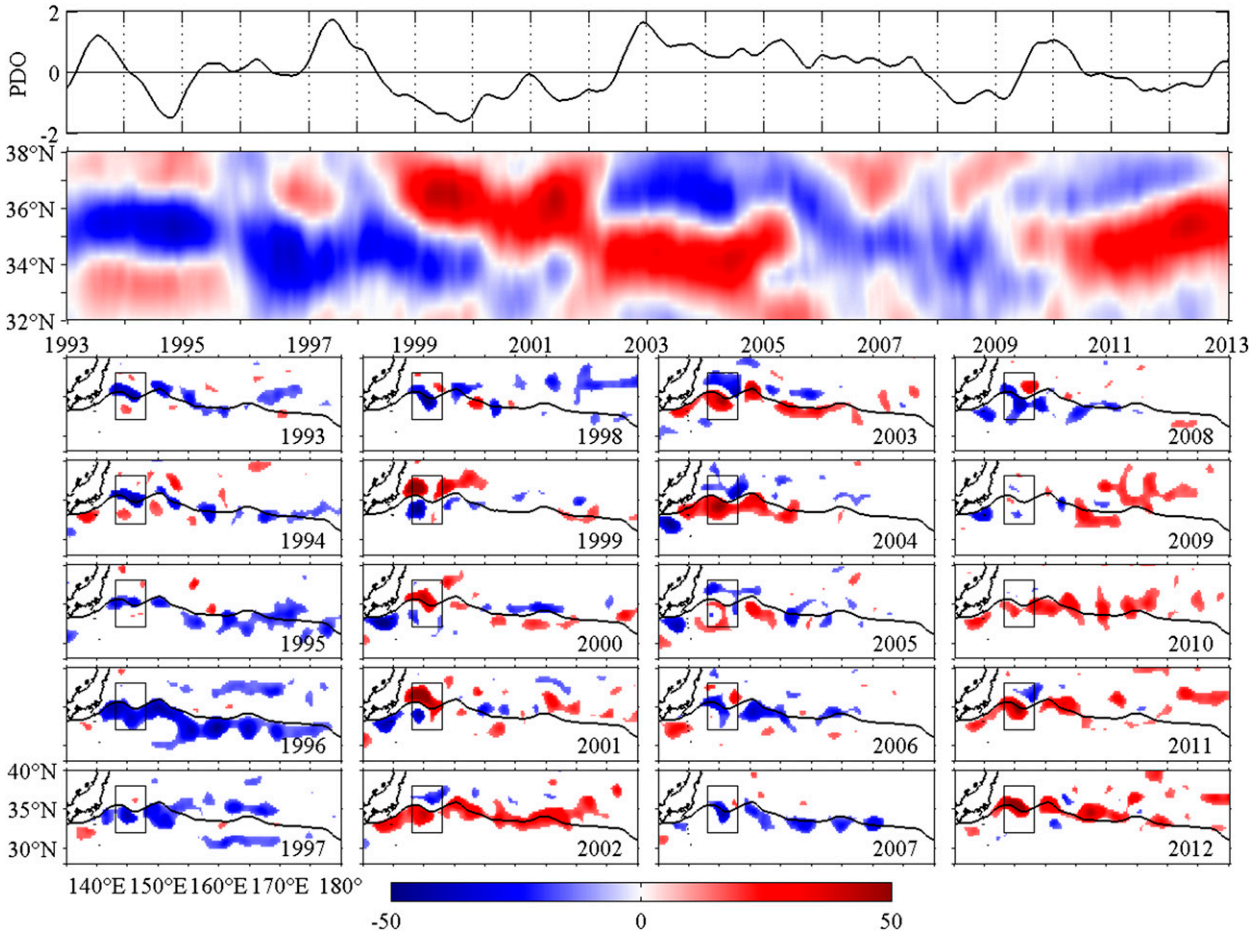

FIG. 13. Annual-mean sea level variability in the Kuroshio Extension region from 1993 to 2012. (top) The detrended and low-pass filtered PDO. (middle) Hovmöller diagram of sea level anomalies as a function of lat and time. Sea levels were low-pass filtered, using a running yearly mean, and zonally averaged over the box shown in the maps below. (bottom) Maps of annual-mean sea level anomaly for each year, 1993–2012. Sea level anomalies with amplitudes less than 12 cm are masked out. The black line shows the path of the mean Kuroshio Extension jet (Fig. 1b).

velocity of Rossby waves is zero (i.e., $\omega_{\max}$). It is interesting to note that the dominant frequency of the HEOF amplitude α_1^{high} is close to $\omega_{\max}$ in the study region, suggesting a physical mechanism for the peak in the plot of $q_1(\omega_0)$ shown in Fig. 5.

The dominant low-frequency HEOF of observed sea level (periods exceeding 350 days) indicates westward-propagating signals on the order of 15 cm along the jet east of the Shatsky Rise and approximately out-of-phase changes on the order of 1 m across the jet in the meander region. One of the advantages of HEOF over EOF is that it can capture propagating and standing patterns in a single mode.

Near the date line, where the jet is broad and weak, the low-frequency sea level changes are predicted well by a linear, forced Rossby wave model in agreement with Qiu (2003). As the signals propagate west, the agreement degrades, particularly in amplitude. Following Sasaki et al. (2013), we explain the disagreement by arguing that the linear Rossby waves are transformed into jet-trapped Rossby waves confined to a few degrees of latitude of the mean jet.

The phase map of $\mathbf{e}_1^{\text{low}}$ indicates that low-frequency changes north of the jet in the meander region may lead changes to the south by about 3 yr. This is supported by a Hovmöller plot of reconstructed sea level, time series of observed sea level from the meander region, and, most importantly, maps of the observed annual-mean sea level anomaly fields (Fig. 13). We attempted to explain the 3-yr anticipation using a combination of thin-jet theory and the rapid barotropic response of the western boundary transport to changes in the large-scale wind field. We recognize that this explanation is highly speculative. We note

that Nakano et al. (2008) recently suggested that the western boundary current generates the northern recirculation gyre (close to B1) through the injection of high potential vorticity created in the viscous sublayer. Previous studies have shown that baroclinic Rossby waves, propagating from the eastern Pacific, do not enter the area north of the jet in the meander region (e.g., Qiu 2003; Nakano and Ishikawa 2010). This may also help explain why the sea level anticipation is observed north of the jet.

One of the difficulties in performing statistical analysis on the North Pacific altimeter dataset is that the observed records are short in comparison to the dominant time scales of variability. Our next step will be to use a high-resolution, fully nonlinear, 3D model of the North Pacific to provide more definitive physical interpretations of the dominant low- and high-frequency HEOFs. Of particular interest will be the role of (i) jet–bathymetry interactions in amplifying the high-frequency sea level variability in the vicinity of the Shatsky Rise and Emperor Seamounts and (ii) variations in western boundary transport on circulation (and sea level) in the meander region. We anticipate that HEOF analysis of model output, similar to the analysis of observed sea level performed here, will be useful in interpreting the results.

Acknowledgments. We thank the two anonymous reviewers for their insightful and constructive comments. We also benefited from discussions with Drs. Yu-Heng Tseng and Youyu Lu. Hongyang Lin and Jianyu Hu were supported by the National Basic Research Program of China (2012CB417402) and the National Natural Science Foundation of China (41276006). Keith Thompson was supported by a Discovery Grant provided by the Natural Sciences and Engineering Research Council of Canada. Hongyang Lin's visit at Dalhousie University was funded by the China Scholarship Council.

APPENDIX A

HEOF Analysis of a Quasigeostrophic Model

A quasigeostrophic (QG) model is now used to help interpret the analysis of observed sea level and illustrate the strengths and weaknesses of HEOF analysis.

The QG model was developed by Hogg et al. (2003). It has three layers and allows for a barotropic response and variable bathymetry. Forcing by the wind and heat flux is steady and obtained from a 110-yr run of a coupled version of the model [version 1.2 of the Quasi-Geostrophic Coupled Model (Q-GCM)]. Two major changes were made to the default parameter settings: the mean thickness of the upper, middle, and bottom layers was changed from 300, 1100, and 2600 m to 700, 1000, and 2300 m; and the Laplacian viscosity coefficient was increased from 0 to 50 $m^2 s^{-1}$, resulting in a more pronounced meandering jet. [See Hogg et al. (2003, 2005) for other parameter settings and a detailed description of the model.]

HEOF analysis was performed on the top-layer streamfunction Ψ_1 in two frequency bands: low frequency (periods longer than 2 yr) and high frequency (periods between 6 months and 1 yr). The dominant low-frequency mode (Fig. A1, left) accounts for 55% of the total variance and describes changes in the strength and path of the jet in the meander region. A similar mode was identified and discussed by Hogg et al. (2005) and related to previous studies (e.g., Simonnet and Dijkstra 2002). The dominant high-frequency mode (Fig. A1, right) accounts for 37% of the total variance and describes large-scale, westward-propagating Rossby waves driven by variations along the eastern boundary. Note that all of the temporal variability of the (spunup) model is internally generated because the external forcing is steady.

The above discussion illustrates two attractive features of HEOF analysis: the modes can change with frequency and propagating patterns can be described by a single mode. HEOF analysis also shares with EOF analysis important limitations. For example, results depend on the study region, the way the data are scaled, and the length of the record (an important concern if the system switches between multiple equilibria; e.g., McCalpin and Haidvogel 1996). The orthogonality of the modes can complicate the physical interpretation of higher-order modes. Finally there is ambiguity in the definition of modes (eigenvectors) with similar eigenvalues.

HEOF analysis has additional limitations. For example, the modes can be very sensitive to the choice of ω_0 and $\delta\omega$. (The wavenumber of the Rossby waves in the eastern part of the QG model domain depends strongly on frequency.)

HEOF analysis has another limitation that is relevant to the present study. Motivated by the propagation of Rossby waves along a line of constant latitude, assume a one-dimensional grid of $2p + 1$ uniformly spaced nodes located at $[-p\Delta, \ldots, p\Delta]$, where Δ is the grid spacing. Assume that sea level varies randomly at the eastern end of the grid and generates a signal that propagates westward at constant speed c and with no change in amplitude. The cross-spectral matrix of the gridpoint sea levels at frequency ω is proportional to $\mathbf{e}\mathbf{e}'$ where $\mathbf{e}' = [e^{-ip\Delta\omega/c}, \ldots, e^{ip\Delta\omega/c}]$.

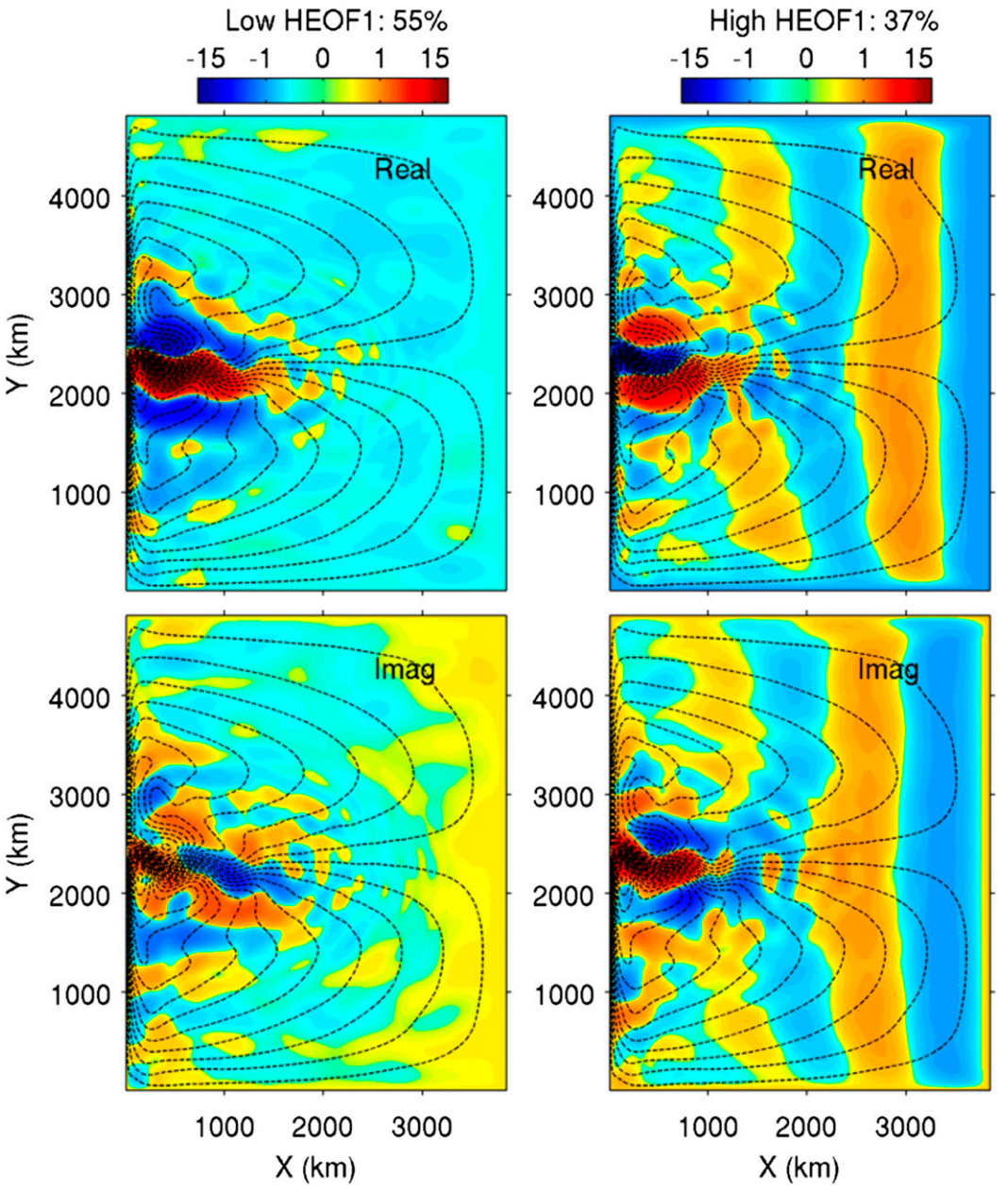

FIG. A1. First HEOF of Ψ_1 from the QG model (appendix A). The colored maps show the (top) real and (bottom) imaginary parts of the first HEOF for periods (left) longer than 2 yr and (right) between 6 months and 1 yr. The dashed contours show the mean of Ψ_1. A nonlinear color scale is used to highlight small-scale changes of Ψ_1 in the eastern part of the domain.

If the easternmost sea level has a narrow spectrum centered on ω_0, the first HEOF for any frequency band containing ω_0 can be approximated by $\mathbf{e}(\omega_0)$. It follows that the elements of this mode will have spatially uniform magnitudes and phases that change linearly with position $p\Delta$ as expected. If the spectrum of the easternmost sea level has two narrowband peaks with equal energy and centered on ω_1 and ω_2, the HEOFs for any frequency band that includes both spectral peaks will be $\mathbf{e}_1 \pm \mathbf{e}_2$, where $\mathbf{e}_{1,2}$ are of the form given above and based on $\omega_{1,2}$. This implies that the amplitude of the HEOFs will depend on position, thereby highlighting the danger of over interpreting the spatial structure of HEOFs, and also estimating phase speeds of propagating waves, in the absence of a narrow spectral peak. This is the reason we conducted sensitivity studies with different $\delta\omega$ in

order to show that the modes calculated from the observations were robust.

APPENDIX B

Statistical Significance of the Complex Correlations

Assume we have two Hilbert-transformed time series of observations with sample correlation ρ_{obs}. To assess the statistical significance of ρ_{obs}, we have adapted the ''wild bootstrap'' technique of Kirch and Politis (2011) to generate independent replicates of the original time series by sampling in the frequency domain. These bootstrap samples are then used to estimate the sampling distribution of the sample correlation estimator $\hat{\rho}$ and the probability that $\hat{\rho}$ will exceed ρ_{obs}, assuming the true correlation ρ is zero.

The wild bootstrap is based on the asymptotic independence, and normality, of the Fourier components of the time series. To calculate bootstrap samples for an observed time series, we used the following scheme:

Step 1: Estimate the power spectral density $f(\omega)$ of the real part of the observed time series. A nonparametric approach was used based on smoothing the periodograms with a Parzen spectral window (e.g., Priestley 1981). The width of the spectral window resulted in 37 equivalent degrees of freedom for each spectral estimate. Additional constraints imposed by possible prefiltering of the original times series (e.g., no energy at periods less than 350 days) were applied to $f(\omega)$.

Step 2: Independently sample from the standard normal distribution to generate normalized real and imaginary parts of the Fourier components of the bootstrap time series at each frequency.

Step 3: Scale the normalized bootstrapped Fourier coefficients at frequency ω by $f(\omega)^{1/2}$ and then inverse Fourier transform to generate a real valued bootstrap time series. (The first three steps correspond to the wild bootstrap applied to the real part of the observed time series.)

Step 4: Hilbert transform the bootstrap time series from Step 3.

The above scheme can be used to generate as many pairs of bootstrap samples as required from the two observed time series, assuming the true correlation is zero. It is then straightforward to calculate (i) squared sample correlations between each pair of bootstrap times series, (ii) the p value (from ρ^2_{obs} and the histogram of sample correlations). If the p value is less than the specified significance level (e.g., 0.05), we conclude the true ρ^2 is greater than zero at the specified significance level.

REFERENCES

Andres, M., J.-H. Park, M. Wimbush, X.-H. Zhu, H. Nakamura, K. Kim, and K.-I. Chang, 2009: Manifestation of the Pacific decadal oscillation in the Kuroshio. *Geophys. Res. Lett.,* **36,** L16602, doi:10.1029/2009GL039216.

——, Y.-O. Kwon, and J. Yang, 2011: Observations of the Kuroshio's barotropic and baroclinic responses to basin-wide wind forcing. *J. Geophys. Res.,* **116,** C04011, doi:10.1029/2010JC006863.

Aoki, S., and S. Imawaki, 1996: Eddy activities of the surface layer in the western North Pacific detected by satellite altimeter and radiometer. *J. Oceanogr.,* **52,** 457–474, doi:10.1007/BF02239049.

——, ——, and K. Ichikawa, 1995: Baroclinic disturbances propagating westward in the Kuroshio Extension region as seen by a satellite altimeter and radiometers. *J. Geophys. Res.,* **100,** 839–855, doi:10.1029/94JC02255.

Barkley, R. A., 1970: The Kuroshio Current. *Sci. J.,* **6,** 54–60.

Barnett, T. P., 1983: Interaction of the monsoon and Pacific trade wind system at interannual time scales. Part I: The equatorial zone. *Mon. Wea. Rev.,* **111,** 756–773, doi:10.1175/1520-0493(1983)111<0756:IOTMAP>2.0.CO;2.

Berloff, P. S., and J. C. McWilliams, 1999: Large-scale, low-frequency variability in wind-driven ocean gyres. *J. Phys. Oceanogr.,* **29,** 1925–1949, doi:10.1175/1520-0485(1999)029<1925:LSLFVI>2.0.CO;2.

Chen, S., 2008: The Kuroshio Extension front from satellite sea surface temperature measurements. *J. Oceanogr.,* **64,** 891–897, doi:10.1007/s10872-008-0073-6.

Cromwell, D., 2006: Temporal and spatial characteristics of sea surface height variability in the North Atlantic Ocean. *Ocean Sci.,* **2,** 147–159, doi:10.5194/os-2-147-2006.

Cushman-Roisin, B., L. Pratt, and E. Ralph, 1993: A general theory for equivalent barotropic thin jets. *J. Phys. Oceanogr.,* **23,** 91–103, doi:10.1175/1520-0485(1993)023<0091:AGTFEB>2.0.CO;2.

Deans, S. R., 1983: *The Radon Transform and Some of Its Applications.* Wiley, 304 pp.

Donohue, K. A., D. R. Watts, K. L. Tracey, A. D. Greene, and M. Kennelly, 2010: Mapping circulation in the Kuroshio Extension with an array of current and pressure recording inverted echo sounders. *J. Atmos. Oceanic Technol.,* **27,** 507–527, doi:10.1175/2009JTECHO686.1.

Ducet, N., P.-Y. Le Traon, and G. Reverdin, 2000: Global high-resolution mapping of ocean circulation from TOPEX/Poseidon and *ERS-1* and *-2*. *J. Geophys. Res.,* **105,** 19 477–19 498, doi:10.1029/2000JC900063.

Ebuchi, N., and K. Hanawa, 2000: Mesoscale eddies observed by TOLEX-ADCP and TOPEX/POSEIDON altimeter in the Kuroshio recirculation region south of Japan. *J. Oceanogr.,* **56,** 43–57, doi:10.1023/A:1011110507628.

Ferry, N., and Coauthors, 2012: GLORYS2V1 global ocean reanalysis of the altimetric era (1993–2009) at meso scale. *Mercator Quarterly Newsletter,* No. 44, Mercator Ocean, Ramonville Saint-Agne, France, 29–39.

Fu, L.-L., and B. Qiu, 2002: Low-frequency variability of the North Pacific Ocean: The roles of boundary- and wind-driven baroclinic Rossby waves. *J. Geophys. Res.,* **107,** 3220, doi:10.1029/2001JC001131.

Gill, A. E., 1982: *Atmosphere–Ocean Dynamics.* Vol. 30. Academic Press, 662 pp.

Greene, A. D., 2010: Deep variability in the Kuroshio Extension. Ph.D. thesis, Graduate School of Oceanography, University of Rhode Island, 150 pp.

Hogg, A. M. C., W. K. Dewar, P. D. Killworth, and J. R. Blundell, 2003: A quasi-geostrophic coupled model (Q-GCM). *Mon. Wea. Rev.,* **131,** 2261–2278, doi:10.1175/1520-0493(2003)131<2261:AQCMQ>2.0.CO;2.

——, P. D. Killworth, J. R. Blundell, and W. K. Dewar, 2005: Mechanisms of decadal variability of the wind-driven ocean circulation. *J. Phys. Oceanogr.,* **35,** 512–531, doi:10.1175/JPO2687.1.

Hurlburt, H. E., A. J. Wallcraft, W. J. Schmitz Jr., P. J. Hogan, and E. J. Metzger, 1996: Dynamics of the Kuroshio/Oyashio current system using eddy-resolving models of the North Pacific Ocean. *J. Geophys. Res.,* **101,** 941–976, doi:10.1029/95JC01674.

Itoh, S., and I. Yasuda, 2010: Characteristics of mesoscale eddies in the Kuroshio–Oyashio Extension region detected from the distribution of the sea surface height anomaly. *J. Phys. Oceanogr.,* **40,** 1018–1034, doi:10.1175/2009JPO4265.1.

Jayne, S. R., and Coauthors, 2009: The Kuroshio Extension and its recirculation gyres. *Deep-Sea Res. I,* **56,** 2088–2099, doi:10.1016/j.dsr.2009.08.006.

Kirch, C., and D. N. Politis, 2011: TFT-bootstrap: Resampling time series in the frequency domain to obtain replicates in the time domain. *Ann. Stat.,* **39,** 1427–1470, doi:10.1214/10-AOS868.

Kwon, Y.-O., M. A. Alexander, N. A. Bond, C. Frankignoul, H. Nakamura, B. Qiu, and L. A. Thompson, 2010: Role of the Gulf Stream and Kuroshio–Oyashio systems in large-scale atmosphere–ocean interaction: A review. *J. Climate,* **23,** 3249–3281, doi:10.1175/2010JCLI3343.1.

Large, W., and S. Pond, 1981: Open ocean momentum flux measurements in moderate to strong winds. *J. Phys. Oceanogr.,* **11,** 324–336, doi:10.1175/1520-0485(1981)011<0324:OOMFMI>2.0.CO;2.

Lin, X., J. Yang, D. Wu, and P. Zhai, 2008: Explaining the global distribution of peak-spectrum variability of sea surface height. *Geophys. Res. Lett.,* **35,** L14602, doi:10.1029/2008GL034312.

McCalpin, J. D., and D. B. Haidvogel, 1996: Phenomenology of the low-frequency variability in a reduced-gravity, quasi-geostrophic double-gyre model. *J. Phys. Oceanogr.,* **26,** 739–752, doi:10.1175/1520-0485(1996)026<0739:POTLFV>2.0.CO;2.

Mizuno, K., and W. B. White, 1983: Annual and interannual variability in the Kuroshio Current system. *J. Phys. Oceanogr.,* **13,** 1847–1867, doi:10.1175/1520-0485(1983)013<1847:AAIVIT>2.0.CO;2.

Mochizuki, T., and Coauthors, 2010: Pacific decadal oscillation hindcasts relevant to near-term climate prediction. *Proc. Natl. Acad. Sci. USA,* **107,** 1833–1837, doi:10.1073/pnas.0906531107.

Nakamura, H., T. Sampe, Y. Tanimoto, and A. Shimpo, 2004: Observed associations among storm tracks, jet streams and midlatitude oceanic fronts. *Earth's Climate, Geophys. Monogr.,* Vol. 147, Amer. Geophys. Union, 329–345, doi:10.1029/147GM18.

Nakano, H., and I. Ishikawa, 2010: Meridional shift of the Kuroshio Extension induced by response of recirculation gyre to decadal wind variations. *Deep-Sea Res. II,* **57,** 1111–1126, doi:10.1016/j.dsr2.2009.12.002.

——, H. Tsujino, and R. Furue, 2008: The Kuroshio current system as a jet and twin ''relative'' recirculation gyres embedded in the Sverdrup circulation. *Dyn. Atmos. Oceans,* **45,** 135–164, doi:10.1016/j.dynatmoce.2007.09.002.

Niiler, P., N. Maximenko, G. Panteleev, T. Yamagata, and D. Olson, 2003: Near-surface dynamical structure of the Kuroshio Extension. *J. Geophys. Res.,* **108,** 3193, doi:10.1029/2002JC001461.

Priestley, M. B., 1981: *Spectral Analysis and Time Series.* Academic Press, 890 pp.

Qiu, B., 2002: The Kuroshio Extension system: Its large-scale variability and role in the midlatitude ocean–atmosphere interaction. *J. Oceanogr.,* **58,** 57–75, doi:10.1023/A:1015824717293.

——, 2003: Kuroshio Extension variability and forcing of the Pacific decadal oscillations: Responses and potential feedback. *J. Phys. Oceanogr.,* **33,** 2465–2482, doi:10.1175/2459.1.

——, and S. Chen, 2005: Variability of the Kuroshio Extension jet, recirculation gyre, and mesoscale eddies on decadal time scales. *J. Phys. Oceanogr.,* **35,** 2090–2103, doi:10.1175/JPO2807.1.

——, and ——, 2010: Eddy-mean flow interaction in the decadally modulating Kuroshio Extension system. *Deep-Sea Res. II,* **57,** 1098–1110, doi:10.1016/j.dsr2.2008.11.036.

——, and ——, 2011: Effect of decadal Kuroshio Extension jet and eddy variability on the modification of North Pacific Intermediate Water. *J. Phys. Oceanogr.,* **41,** 503–515, doi:10.1175/2010JPO4575.1.

——, K. A. Kelly, and T. M. Joyce, 1991: Mean flow and variability in the Kuroshio Extension from *Geosat* altimetry data. *J. Geophys. Res.,* **96,** 18 491–18 507, doi:10.1029/91JC01834.

——, S. Chen, P. Hacker, N. G. Hogg, S. R. Jayne, and H. Sasaki, 2008: The Kuroshio Extension northern recirculation gyre: Profiling float measurements and forcing mechanism. *J. Phys. Oceanogr.,* **38,** 1764–1779, doi:10.1175/2008JPO3921.1.

Rhines, P., and F. Bretherton, 1973: Topographic Rossby waves in a rough-bottomed ocean. *J. Fluid Mech.,* **61,** 583–607, doi:10.1017/S002211207300087X.

Saha, S., and Coauthors, 2010: The NCEP Climate Forecast System Reanalysis. *Bull. Amer. Meteor. Soc.,* **91,** 1015–1057, doi:10.1175/2010BAMS3001.1.

Sasaki, Y. N., and N. Schneider, 2011: Decadal shifts of the Kuroshio Extension jet: Application of thin-jet theory. *J. Phys. Oceanogr.,* **41,** 979–993, doi:10.1175/2010JPO4550.1.

——, S. Minobe, and N. Schneider, 2013: Decadal response of the Kuroshio Extension jet to Rossby waves: Observation and thin-jet theory. *J. Phys. Oceanogr.,* **43,** 442–456, doi:10.1175/JPO-D-12-096.1.

Schmeits, M. J., and H. A. Dijkstra, 2002: Subannual variability of the ocean circulation in the Kuroshio region. *J. Geophys. Res.,* **107,** 3235, doi:10.1029/2001JC001073.

Sheu, W.-J., C.-R. Wu, and L.-Y. Oey, 2010: Blocking and westward passage of eddies in the Luzon Strait. *Deep-Sea Res. II,* **57,** 1783–1791, doi:10.1016/j.dsr2.2010.04.004.

Simonnet, E., and H. A. Dijkstra, 2002: Spontaneous generation of low-frequency modes of variability in the wind-driven ocean circulation. *J. Phys. Oceanogr.,* **32,** 1747–1762, doi:10.1175/1520-0485(2002)032<1747:SGOLFM>2.0.CO;2.

Taguchi, B., Y. Yoshikawa, H. Mitsudera, and H. Nakamura, 2000: Oceanic variability in the Kuroshio Extension: Comparison between the Kuroshio/Oyashio system model results and the TOPEX/POSEIDON altimetry data (in Japanese with English abstract). *Rep. Japan Mar. Sci. Tech. Center,* **40,** 145–160.

——, S.-P. Xie, H. Mitsudera, and A. Kubokawa, 2005: Response of the Kuroshio Extension to Rossby waves associated with the 1970s climate regime shift in a high-resolution ocean model. *J. Climate,* **18,** 2979–2995, doi:10.1175/JCLI3449.1.

——, ——, N. Schneider, M. Nonaka, H. Sasaki, and Y. Sasai, 2007: Decadal variability of the Kuroshio Extension: Observations and an eddy-resolving model hindcast. *J. Climate,* **20,** 2357–2377, doi:10.1175/JCLI4142.1.

Tai, C.-K., and W. B. White, 1990: Eddy variability in the Kuroshio Extension as revealed by *Geosat* altimetry: Energy propagation away from the jet, Reynolds stress, and seasonal

cycle. *J. Phys. Oceanogr.,* **20,** 1761–1777, doi:10.1175/1520-0485(1990)020<1761:EVITKE>2.0.CO;2.

Tatebe, H., and I. Yasuda, 2001: Seasonal axis migration of the upstream Kuroshio Extension associated with standing oscillations. *J. Geophys. Res.,* **106,** 16 685–16 692, doi:10.1029/2000JC000467.

Thompson, K. R., and E. Demirov, 2006: Skewness of sea level variability of the world's oceans. *J. Geophys. Res.,* **111,** C05005, doi:10.1029/2004JC002839.

Tracey, K. L., D. R. Watts, K. A. Donohue, and H. Ichikawa, 2012: Propagation of Kuroshio Extension meanders between 143° and 149°E. *J. Phys. Oceanogr.,* **42,** 581–601, doi:10.1175/JPO-D-11-0138.1.

von Storch, H., and F. W. Zwiers, 1999: *Statistical Analysis in Climate Research.* Cambridge University Press, 484 pp.

Wang, L., C. J. Koblinsky, and S. Howden, 1998a: Annual and intra-annual sea level variability in the region of the Kuroshio Extension from TOPEX/Poseidon and *Geosat* altimetry. *J. Phys. Oceanogr.,* **28,** 692–711, doi:10.1175/1520-0485(1998)028<0692:AAIASL>2.0.CO;2.

——, ——, ——, and B. Beckley, 1998b: Large-scale Rossby wave in the mid-latitude South Pacific from altimetry data. *Geophys. Res. Lett.,* **25,** 179–182, doi:10.1029/97GL03567.

Waterman, S., N. G. Hogg, and S. R. Jayne, 2011: Eddy–mean flow interaction in the Kuroshio Extension region. *J. Phys. Oceanogr.,* **41,** 1182–1208, doi:10.1175/2010JPO4564.1.

Yasuda, I., 2003: Hydrographic structure and variability in the Kuroshio–Oyashio transition area. *J. Oceanogr.,* **59,** 389–402, doi:10.1023/A:1025580313836.